

Interannual Temperature Events and Shifts in Global Temperature: A “Multiwavelet” Correlation Approach

Jeffrey Park, Department of Geology and Geophysics, Yale University, New Haven, Connecticut

E-mail: jeffrey.park@yale.edu

Michael E. Mann, Department of Geosciences, University of Massachusetts, Amherst, Massachusetts

PAPER ID: 3-003

ABSTRACT: For the purpose of climate signal detection, we introduce a method for identifying significant episodes of large-scale oscillatory variability. The method is based on a multivariate wavelet algorithm that identifies coherent patterns of variation simultaneously within particular ranges of time and periodicity (or frequency) that may vary regionally in the timing and amplitude of the particular temperature oscillation. By using this methodology, an analysis is performed of the instrumental record of global temperatures spanning the past 140 years. The duration of an “episode” is chosen to correspond to 3–5 cycles at a specified oscillation period, which is useful for detecting signals associated with the global El Niño/Southern Oscillation (ENSO) phenomenon. To confirm the robustness of signals detected in the earliest, sparse data (only 111 5° longitude by 5° latitude grid points are available back to 1854), we performed multiple analyses overlapping in time, using increasingly dense subsets of the full (1570 grid point) temperature data. In every case, significant interannual episodes are centered in the 3–7 year period range corresponding to the conventional band of ENSO-related variance and describe intervals of quasi-oscillatory variability of decadal-scale duration. These episodes consist of a sequence of one or two warm and cold events with sea surface temperature fluctuations in the eastern tropical Pacific of amplitude $\pm 0.6^{\circ}$ – 1.1° C. Each episode includes one or more historically prominent El Niño events. The signals are characterized as significant, however, by virtue of their global-scale pattern of temperature variations as well as their oscillatory pattern in time. The 1920–1940 interval of increasing global temperatures was bracketed by oscillatory

episodes with unusual global patterns of expression relative to the recent ENSO episodes of the 1970s and 1980s. The episodes that preceded the 1920–1940 and 1975–present intervals of rapid warming were associated with globally averaged temperature fluctuations of $T_{GLB} > 0.4^{\circ}\text{C}$, the largest among those identified. In contrast, the episode that concludes the 1920–1940 temperature rise exhibits a global-mean fluctuation $T_{GLB} = 0.05^{\circ}\text{C}$, smallest among the observed episodes. These observations motivate speculation about the possible relationship between ENSO variability and global warming, in particular, the relationship between ENSO and the transient storage of heat in the tropical upper ocean layer, and the relationship between secular climate change and the amplitude of interannual ENSO events.

[KEYWORDS: Climate dynamics; Climate and interannual variability; Ocean/atmosphere interactions; El Niño]

Copyright: ©1999 Earth Interactions ¹

1. Introduction

The erratic progression of 20th century warming over time complicates attempts to identify a causal link with an anthropogenic enhanced-greenhouse effect. The Northern Hemisphere (NH) mean temperature series indicates a long-term warming trend, but with distinct intervals of rapid warming, stasis, and even slight cooling. In contrast, a steady increase in atmospheric carbon dioxide levels has been observed since the dawn of industrialization. It has been debated whether the complex, but increasing, trend in global-mean temperature reflects simply a large natural excursion of the climate or the erratic path of surface temperatures within the context of an anthropogenic warming. The best available evidence supports the latter proposition (e.g., [Intergovernmental Panel on Climate Control \(IPCC\), 1996](#); [Hegerl et al., 1997](#); [Mann et al., 1998](#)).

Natural variability, intrinsic to the climate system, may mask a simple response to anthropogenic greenhouse forcing. Some of the anomalous global warmth of the 1980s has been at least partly associated with an interdecadal excursion of the climate (e.g., [Trenberth, 1990](#); [Trenberth and Hurrell, 1994](#); [Graham, 1994](#)) that may represent a natural oscillatory mode of the coupled ocean-atmosphere system ([Latif and Barnett, 1994](#); [Robertson, 1996](#); [Ghil and Vautard, 1991](#); [Mann and Park, 1996](#)). Certainly, El Niño/Southern Oscillation (ENSO), itself an intrinsic climate process, has significantly contributed to the warmth of the 1990s. However, this enhanced ENSO-related warmth might itself be anthropogenic in nature ([Trenberth and Hoar, 1996](#)) though not without dispute ([Rajagopalan et al., 1998](#)). On the multidecadal (50–70 year) timescales of particular relevance for assessing a response to climate forcing, there is empirical instrumental ([Kushnir, 1994](#); [Mann and Park, 1994](#);

[Schlesinger and Ramankutty, 1994](#)) long-term climate proxy ([Mann et al., 1995](#)) and model-based ([Delworth et al., 1993](#)) evidence for intrinsic oscillatory climate processes that may compete on the timescales of the forcing. The best evidence, however, is that these processes are associated with regional changes in ocean circulation ([Delworth et al., 1993](#)) that largely redistribute heat over the surface of the globe ([Mann and Park, 1994](#); [Mann et al., 1995](#)), projecting weakly onto global or even hemispheric warmth.

The observed asymmetry in the warming might have nongreenhouse external forcing factors to blame, both natural and anthropogenic. Many have attributed at least some of the asymmetry in the global warming trend to aerosol cooling superimposed on a greenhouse warming signal (e.g., [IPCC, 1996](#); [Hegerl et al., 1997](#)) though a thoroughly satisfying physical basis for aerosol radiative effects is not yet available. There is some evidence that warming from the early 19th century through the early part of this century may be attributed at least in part to increasing solar irradiance ([Lean et al., 1995](#); [Mann et al., 1998](#)). The acceleration of warming through the 1990s, however, appears to be unprecedented in the Northern Hemisphere for at least six centuries ([Mann et al., 1998](#)) and may indeed indicate an emerging anthropogenic greenhouse signal.

We consider in this study yet another possible alternative for the asymmetric pattern of global warming this century, that anthropogenic forcing may interact strongly with the character of intrinsic ENSO-related climate variability. Cane et al. ([Cane et al., 1997](#)) argue that the observed global warming, which is somewhat muted relative to typical estimates of the expected response to anthropogenic greenhouse forcing, may reflect a negative feedback from the same intrinsic tropical Pacific coupled ocean-atmosphere dynamics that govern ENSO. They demonstrate a significant lag between the forcing and response, associated with ocean dynamics. Trenberth and Hoar ([Trenberth and Hoar, 1996](#)) argue, by contrast, for a statistical relationship between the anomalously persistent warm episode of the early 1990s and greenhouse warming. Such a relationship implies feedbacks, potentially nonlinear in nature, that are not as yet well understood, though some models display limited evidence for enhanced El Niño-like conditions in an anthropogenic enhanced greenhouse scenario ([Meehl and Washington, 1996](#); [Knutson et al., 1997](#)). Indeed, if much of the heat energy associated with an enhanced greenhouse is stored in the low-latitude oceans, tropical ocean-atmosphere dynamics could significantly modulate the progress of anthropogenic climate change (e.g., [Gu and Philander, 1997](#)). This paper reports an empirical study of short-lived oscillatory global patterns of temperature variation that reveals potential links between ENSO-scale variability and longer-term trends in global temperature over the instrumental period.

A variety of statistical models have been applied to global temperature data in search of significant oscillatory patterns of variation (e.g., [Mann and Park, 1993](#); [Mann and Park, 1994](#); [Allen and Smith, 1994](#)). Mann and Park ([Mann and Park, 1994](#)) found, in addition to significant secular variations, evidence for quasi-oscillatory patterns of variation in global temperature grid-point anomaly data on interdecadal (16–18 year), quasi-decadal (10–11 year), and interannual “ENSO band” (3–7 year) timescales. The multiple-taper time-series

method coupled with the singular-value decomposition (hereinafter denoted MVM-STD) can be used to detect and reconstruct these signals (see the review by [Mann and Park, 1999](#)) is a frequency-domain variant on empirical orthogonal function (EOF) analysis ([Mann and Park, 1994](#); [Mann et al., 1995](#); [Mann and Park, 1996](#)) that makes use of multiple discrete Fourier transforms (DFTs) of each grid-point series within a given narrow frequency band. Statistical independence among the multiple DFT spectrum estimates is afforded by a family of orthogonal data tapers ([Thomson, 1982](#); [Park et al., 1987](#)). The MTM-SVD method allows for the detection of amplitude- and phase-modulated oscillatory climate signals with regionally varying patterns of amplitude and phase that evolve over a typical cycle. Detection confidence is estimated relative to the null hypothesis of spatially correlated colored noise. Implicit in this approach are nonetheless some potentially restrictive assumptions when applied to long datasets. The statistical model of “climate signals” demands a narrowband character with spatial patterns of relative phase and amplitude that are consistent from an oscillatory episode to oscillatory episode. This assumption was relaxed in an “evolutionary” generalization of the MTM-SVD method (see [Mann et al., 1995](#); [Mann and Park, 1996](#); [Mann and Park, 1999](#)) in which the analysis was performed in successive overlapping data windows to capture slow changes in significant oscillatory spatiotemporal patterns of variation in climate data.

An evolutionary analysis sacrifices narrowband resolution in the frequency domain for increased time resolution. If this resolution trade-off is pushed further, spatially correlated variability in an instrumental data archive can be represented as a set of discrete oscillatory climate episodes, each with a preferred timescale. Wavelet cross-correlation methods can be adapted to investigate episodic oscillatory behavior on a range of timescales. As with the MTM-SVD method of Mann and Park ([Mann and Park, 1994](#); [Mann and Park, 1999](#)), we can reconstruct such episodes in both space and time. In [section 2](#) we outline a multivariate wavelet correlation algorithm that includes a method to reconstruct the spatial pattern of relative amplitude and phase of the inferred signal. In [section 3](#) we apply this algorithm to the instrumental record of global grid-point temperature anomaly data ([Jones and Briffa, 1992](#)) to investigate episodically correlated temperature variability in the instrumental record.

Rather than interrogate the global temperature anomaly dataset for a known or suspected climate signal, the exploratory statistical approach of this study determines from the data itself the timescales of possible signals and the time intervals during which climatic signals are evident. The likelihood of “false positives” can be quite significant. Nonparametric significance tests invoking an appropriate null hypothesis can guide confidence in the likelihood that detected signals could have arisen from statistical coincidence. Nonetheless, prudence demands that a variety of self-consistency checks be made and that unexpected “signals” in the data be cautiously interpreted.

2. Slepian Wavelets

We apply a wavelet-based multivariate correlation estimator based on the singular value decomposition (SVD). Although the algorithm is new, it is closely related to more familiar multivariate EOF techniques. Rather than analyzing correlations (e.g., [Trenberth and Shea, 1987](#)) or spectral coherences (e.g., [Mann and Park, 1993](#)) between many pairs of records to assess the patterns of large-scale climate signals, multivariate SVD-based techniques compute single patterns in space and time that correlate multiple data records. With multivariate techniques based on the Fourier transform (e.g., [Mann and Park, 1994](#)) one can estimate frequency-dependent patterns of correlation. A short sliding time window can detect time-varying coherent structure in the data, but wavelet-based techniques have a potential advantage: the time interval analyzed is proportional to the “center period” of the wavelet. This allows transient signals on a wide range of timescales to be assessed on an equal basis, with an fixed number of cycles throughout. Wavelet-based methods are not the optimal choice for studying truly narrowband climate signals. This includes the seasonal cycle in temperature and, perhaps, some of the persistent signals identified in the previous analyses of Mann and Park ([Mann and Park, 1993](#); [Mann and Park, 1994](#); [Mann and Park, 1996](#)).

Many popular wavelet functions average spectral information over a broad range of frequencies, e.g., the functions used in the fast-wavelet transform of Daubechies ([Daubechies, 1992](#)). Although averaging of spectral information is unavoidable, wavelets designed to optimize computational speed or functional simplicity often suffer extreme spectral leakage bias. Lilly and Park ([Lilly and Park, 1995](#)) describe how to design wavelets that, though broadband in character, have optimal band-limiting properties. A given choice of frequency resolution (the time-bandwidth product p_w) and number of cycles (the time-bandcenter product p_c) describes a family of mutually orthogonal “Slepian” wavelets that can be used for the cross correlation of multivariate times series. A set of M -point Slepian wavelets with optimal frequency concentration is defined by extremizing the functional

$$\lambda(M, f_c, f_w) = \frac{\int_{f_c - f_w}^{f_c + f_w} |W(f)|^2 df + \int_{-f_c - f_w}^{-f_c + f_w} |W(f)|^2 df}{\int_{-1/2}^{1/2} |W(f)|^2 df} \quad (1)$$

where Δt is the sampling interval and

$$W(f) = \sum_{m=0}^{M-1} w_m e^{i2\pi f m \Delta t} \quad (2)$$

is the discrete Fourier transform of the wavelet $\{w_m\}_{m=0}^{M-1}$. **Figure 1** illustrates the relation between the frequency parameters f_c, f_w and the center period $T_c=1/f_c$.

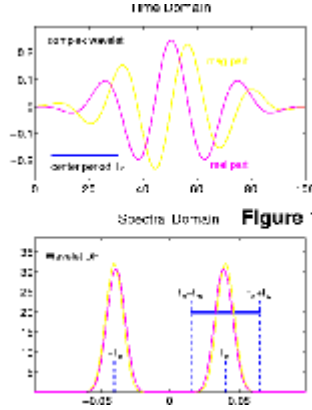


Figure 1. Relationship between time- and spectral-domain parameters that govern the Slepian wavelets. For a given oscillatory period T_c , corresponding to center frequency $f_c = 1/T_c$, a family of wavelets can be computed whose discrete Fourier transforms (DFTs) are optimally bandlimited within the frequency intervals $(-f_c - f_w, -f_c + f_w)$ and $(f_c - f_w, f_c + f_w)$. To specify a collection of approximately self-similar wavelet families, the user fixes a dimensionless time-bandcenter product $p_c = f_c T$ and time-bandwidth product $p_w = f_w T$, where T is the duration of a wavelet family. As the wavelet duration T is varied, f_c and f_w vary so that the number of center-period oscillations in each wavelet is p_c . The complex-valued wavelet shown corresponds to time-bandwidth product $p_w = 2.5$ and time-bandcenter product $p_c = 4.0$. [Click on icon ² (approx 11.8 kbyte) to view full figure.]

The time-bandwidth product p_w is an adjustable parameter in multiple-taper time-series methods (Thomson, 1982; Park et al., 1987; Kuo et al., 1990; Mann and Park, 1994; Mann and Lees, 1996) that determines the trade-off between narrowband resolution in the frequency domain and the variance of spectrum estimates. For instance, if $p_w = 3$, a wavelet with duration $M\Delta t = 10$ years will be sensitive primarily to variability in a frequency range $2f_w$, where $f_w = p_w/M\Delta t = 0.3$ cycles per year. The time-bandcenter product p_c scales the number of oscillations with period $T_c = 1/f_c$ that are contained in a wavelet of duration $M\Delta t$. If the wavelet duration $M\Delta t = 10$ years and the time-bandcenter product $p_c = 4$, then the wavelet's center period $T_c = 10/4 = 2.5$ years. A sequence of mutually orthogonal wavelets

$\psi^{(0)}, \psi^{(1)}, \psi^{(2)}, \dots, \psi^{(K)}$ can be calculated from the extremal values of (1) by using (2) to transform the relation into a matrix eigenvalue problem. The wavelets appear in odd/even function pairs, ordered by decreasing frequency-concentration parameter λ . In practice, pairs of odd and even wavelets in this sequence have comparable frequency concentration. In order to study phase delays in episodic signals, Lilly and Park ([Lilly and Park, 1995](#))

combined odd/even wavelet pairs into complex-valued wavelets $\tilde{\psi}^{(k)} = (\psi^{(k)} \pm i\psi^{(k+1)})/\sqrt{2}$, where the real part is an even wavelet, the imaginary part is the odd wavelet, and the sign is chosen to match the $e^{-i2\pi ft}$ phase convention.

The Slepian wavelets are mutually orthogonal, so that the transforms with different wavelets are statistically independent when evaluated at identical time-frequency points. The ability to treat transform values from different wavelets as independent random variables is the main rationale for using the multiple-wavelet or “multiwavelet” algorithm for cross correlation. In the data analysis, we used $K = 3$ complex-valued wavelets in each frequency band, using $p_w = 2.5$ and $p_c = 4$ ([Figure 2](#)). These choices prescribe a resolution/variance trade-off similar to the multiple-taper SVD (“MTM-SVD”) analysis of Mann and Park ([Mann and Park, 1994](#); [Mann and Park, 1996](#)).

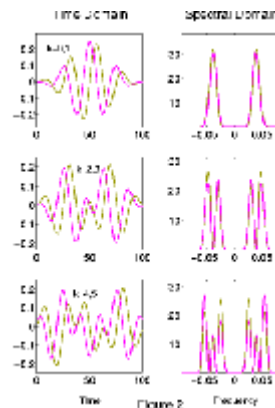


Figure 2. The first six Slepian wavelets, optimized for frequency concentration, with time-bandwidth product $p_w = 2.5$ and time-bandcenter product $p_c = 4.0$. The odd and even discrete wavelet functions are grouped into three complex valued wavelets in order to capture phase delays in temperature signals between gridpoint data series. The purple lines denote even-wavelets (real-part of complex-valued wavelets). The yellow lines denote odd-wavelets (imaginary part of complex-valued wavelets). [Click on icon ³ (approx 18.4 kbyte) to view full figure.]

Lilly and Park ([Lilly and Park, 1995](#)) used an SVD of Slepian wavelets to detect seismic waves in three-component seismograms, and Bear and Pavlis ([Bear and Pavlis, 1997](#)) have extended the method to arrays of seismic sensors. To apply these methods in a climate

context, we redefine the appropriate “spatial” degrees of freedom. In seismic data analysis, there are $M = 3$ spatial coordinates that describe ground motion. In the instrumental temperature data, there are $M \sim 300\text{--}1600$ geographic grid points that contribute to the multiwavelet transform matrix $\mathbf{X}(f_c, n\Delta t)$, depending on the time interval in question. For each grid-point time series we remove the mean and normalize the series to unit variance before analysis. The kj th entry of this matrix is the convolution of the k th complex Slepian wavelet with the j th data series $\{x^{(j)}(n\Delta t)\}_{n=1}^N$

$$\{\mathbf{X}(f_c, n\Delta t)\}_{kj} = \sum_{m=0}^{M-1} \tilde{\psi}_m^{(k)*} x^{(j)} [(n - M/2 + m) \Delta t] \quad (3)$$

The asterisk denotes complex conjugation. The SVD is $\mathbf{X} = \mathbf{U} \cdot \mathbf{D} \cdot \mathbf{V}^H$, where \mathbf{U} is a 3×3 unitary matrix, \mathbf{V}^H is a $3 \times M$ matrix of mutually orthogonal rows, and \mathbf{D} is a 3×3 diagonal matrix. The superscript H denotes Hermitian conjugate. The first three diagonal elements of \mathbf{D} , denoted $d^{(j)}$, $j = 1, 2, 3$, are the singular values of \mathbf{X} with $d^{(1)} \geq d^{(2)} \geq d^{(3)} \geq 0$. The columns of \mathbf{U} and \mathbf{V} correspond to, respectively, eigenvectors $\hat{\mathbf{u}}^{(j)}$ of the 3×3 matrix $\mathbf{X} \cdot \mathbf{X}^H$ and the three nontrivial eigenvectors $\hat{\mathbf{v}}^{(j)}$ of the $M \times M$ matrix $\mathbf{X}^H \cdot \mathbf{X}$. The $\hat{\mathbf{u}}^{(j)}$ and the $\hat{\mathbf{v}}^{(j)}$ are the left and right singular vectors of \mathbf{X} , respectively. For simplicity below, we refer to these singular-vector pairs collectively as an “eigenvector” of \mathbf{X} .

If $d^{(1)} \gg d^{(2)}, d^{(3)}$, most of the temperature variability in a particular region of the time-frequency plane is explained by a single (the “principal”) eigenvector. The statistic $\hat{d}^{(1)}$ is thus used as a signal detection parameter, while the left and right eigenvectors of the correlation matrix \mathbf{X} can be used to reconstruct the associated spatiotemporal signal. We interpret the singular vectors associated with $d^{(1)}$ as empirical orthogonal functions (EOFs) for time-limited, frequency-concentrated data variability. The spatial EOF is given by $\hat{\mathbf{v}}^{(1)}$, describing the relative spatial pattern of amplitude and phase relationships between grid points with its complex-valued components. The time-domain EOF $\hat{\mathbf{u}}^{(1)}$ specifies a time history with a linear combination of the complex Slepian wavelets $\tilde{\psi}^{(k)}$. Combined with the relative amplitude and phase in the components of the “spatial” singular vector $\hat{\mathbf{v}}^{(1)}$, one can reconstruct at each grid point the spatiotemporal signal associated with a particular eigenvector of \mathbf{X} .

To estimate the statistical significance of a putative signal, we compare the fractional

variance explained by the principal eigenvector within a given band, $\bar{d}^{(1)} = (d^{(1)})^2 / \sum_{j=1}^K (d^{(j)})^2$. Random excursions of this parameter become more rare as the spatial degrees of freedom increase in number, and confidence limits for significance can be readily obtained by both parametric and nonparametric means (see [Mann and Park, 1994](#); [Mann and Park, 1996](#); [Mann and Park, 1999](#)). For the number of spatial degrees of freedom \bar{M} present in the global temperature (between 20 and 40 according to Mann and Park ([Mann and Park, 1994](#))), typically a little more than half the normalized data variance needs to be described by the principal eigenvector (i.e., $\bar{d}=0.5$) for it to achieve a 90% significance level. A 99% confidence is achieved if 55% of the normalized variance is described. More careful empirical significance levels can be calculated from a nonparametric bootstrap procedure (see [Mann and Park, 1996](#); [Mann and Park, 1999](#)) based on the assumption of a spatially correlated process with a smoothly varying colored noise spectrum. This assumption has been shown to be valid even for the reddest spectra encountered in instrumental grid-point temperature series ([Mann et al., 1999](#)). We applied a similar Monte Carlo procedure to establish significance in the multiwavelet analysis. Caveats are required due to the poorer frequency-domain localization of the wavelets and are described in more detail in [section 3](#).

In our terminology, a half-cycle interval of anomalous warming or cooling is termed an “event.” An “episode” is a sequence of prominent temperature cycles that exhibit a nonrandom degree of spatiotemporal correlation. The multiwavelet algorithm for detecting and reconstructing episodes that contain one or several prominent ENSO events rests only on the criterion that they lead to an anomalous degree of spatial coherence in the data at a preferred timescale for one or a few cycles. This relaxes the more familiar paradigms that ENSO events are phase-locked to the annual cycle and are of fixed duration (e.g., [Ropelewski and Halpert, 1987](#); [Halpert and Ropelewski, 1992](#)) or that ENSO variability is confined to fixed frequency bands of variability (e.g., [Barnett, 1991](#); [Mann and Park, 1993](#); [Mann and Park, 1994](#)). Despite greater flexibility, the methodology has limitations. In particular, a linear spatial relationship is posited between grid points over the globe in the description of any particular signal. The signal can vary regionally in phase and amplitude but is described globally by the same family of wavelet basis functions. In regions where dynamical feedbacks are particularly important, the local amplitude of the signal may in fact be related nonlinearly to the large-scale signal. In the case of ENSO, we might expect that temperature variations in midlatitude continental regions are linearly correlated with each other, as they are mediated primarily through linear dynamical influences such as anomalous advection of sensible heat. In contrast, in areas of the eastern tropical Pacific, where upwelling responses and wind-induced surface cooling are particularly prominent during the evolution of an event, temperature variations may be nonlinearly amplified relative to the large-scale signal. Despite these limitations, our criteria for a significant episode of oscillatory large-scale variability can nonetheless provide a powerful new tool for investigating ENSO and other oscillatory climate phenomena. The particular evolving patterns of significant interannual episodes and their histories over time provide novel

inferences into possible mechanisms that relate ENSO with long-term climate change.

3. Episodes of Correlated Temperature Variability

To study global-scale temperature patterns, we make use of gridded (5° longitude \times 5° latitude) monthly temperature anomaly data available back to 1854, as described by Jones and Briffa ([Jones and Briffa, 1992](#)). These data have been corrected for urban heat bias and other known systematic nonclimatic influences. The reader is referred to Jones and Briffa ([Jones and Briffa, 1992](#)) for a discussion of these corrections and possible biases. It should nonetheless be kept in mind that imperfect correction for certain nonclimatic factors, such as historical changes in bucket measurements of sea surface temperatures (e.g., [Bottomley et al., 1990](#)), could lead to abrupt changes in the statistical properties of the data that might appear as spurious correlated episodes. This effect is similar to spurious correlations seen near the endpoints of the data interval where boundary effects influence the analysis and will be discussed later.

To avoid problems associated with inhomogeneous temporal sampling, we used grid-point data series containing only small gaps (none longer than 3 months) between 1854 and 1993. We interpolated these gaps linearly. A more stringent restriction to grid-point series with only 1-month gaps did not change the analysis significantly. Because spatial coverage increases with time, we examined six overlapping time intervals 1854–1993 ($M = 111$ grid points), 1884–1993 ($M = 368$), 1904–1993 ($M = 500$), 1924–1993 ($M = 663$), 1944–1993 ($M = 898$), 1964–1993 ($M = 1570$). For each grid-point time series we remove the mean and normalize the series to unit variance before analysis. Normalization tends to downweight the otherwise inflated influence of high-latitude and continental interior grid points, which are subject to large wintertime variance, and to increase the influence of maritime grid points, where high-frequency variability is restrained by the ocean's thermal inertia. The contributions of grid points were also area-weighted to assure more homogeneous regional representation.

We performed the multiwavelet analysis—calculating wavelet transforms of the grid-point data series and applied the SVD-based coherence estimation approach to identify “regions” in the time-frequency plane where high-amplitude, spatially coherent variations are evident in the global temperature data. The normalized first singular values $\tilde{d}^{(1)}$ are plotted as a function of time and periodicity for three of the analyzed time intervals in [Figure 3](#). Only results for the period range 0.5–20 years are shown. Signals with timescales longer than 20 years are not resolvable from a secular trend. As discussed previously, correlations are artificially inflated near the endpoints of the data series, where the interval analyzed extends past the data boundaries (beyond which the temperature “anomalies” are identically zero). Consistency among the different analyses is good, suggesting that correlation in the sparser datasets is a reliable indicator of more densely sampled data. However, certain features (such

as the peak of $\tilde{d}^{(1)}$ near 1984 at $T_c \cong 3$ year, corresponding to the notorious 1982–1983 and 1986–1987 El Niño and 1988–1989 La Niña events) are most evident in the most recent 1964–1993 dataset, which samples the tropical Pacific most densely. [Table 1](#) summarizes the statistical properties of these episodes. The ENSO-related episodes are discussed in more detail in [section 4](#). A few prominent “quasi-annual” episodes (associated with peaks of $\tilde{d}^{(1)} > 0.6$ at wavelet periods $0.5 < T_c < 1.0$ year) also appear in the data ([Figure 3](#), top) centered on the years 1906, 1945, and 1962.5. These detection peaks weaken in prominence as tropical data coverage becomes dense in the shorter datasets, indicating a largely midlatitude expression of the signals. The statistical significance of these apparent “quasi-annual” signals is questionable, however, as explained below.

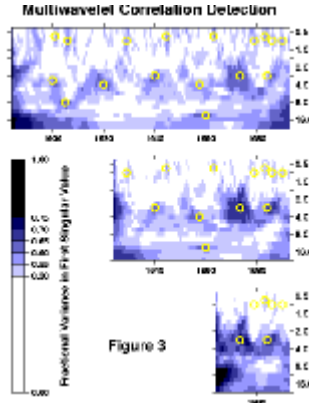


Figure 3. Time-frequency plot of significant global surface-temperature episodes, as flagged by maxima in $\tilde{d}^{(1)}$, the normalized first singular value of multiwavelet correlation matrices. Yellow circles mark local maxima in $\tilde{d}^{(1)}$ at which wavelet reconstructions were performed. Such a matrix is computed and decomposed for each bank of wavelets at time intervals of 0.5 year. If a “large” proportion of variance is explained by the first singular-vector pair $\hat{\mathbf{v}}^{(1)}, \hat{\mathbf{u}}^{(1)}$ of the matrix, a nonrandom correlation can be posited. The “wavelet period” denotes the dominant oscillation period, in years, of an episode of correlated temperature variation. Edge effects contaminate the start and end of the data intervals, leading to spuriously large correlations. Calculations for three data intervals are shown, using fixed global data grids in each: 1884–1993 ($M = 368$ grid points), 1924–1993 ($M = 663$ grid points), and 1964–1993 ($M = 1570$ grid points). Monte Carlo estimates for multivariate white noise with $\hat{M} = 20$ spatial degrees of freedom give the following approximate confidence levels for nonrandom correlation: 90% for $\tilde{d}^{(1)} > 0.50$, 95% for $\tilde{d}^{(1)} > 0.52$, and 99% for $\tilde{d}^{(1)} > 0.55$, while a bootstrap resampling approach slightly more conservative bounds (90% for $\tilde{d}^{(1)} > 0.52$, 95% for $\tilde{d}^{(1)} > 0.535$, and 99% for $\tilde{d}^{(1)} > 0.575$). The result of a

more appropriate significance level estimation procedure, taking serial correlation explicitly into account, is shown below in [Figure 4](#). [Click on icon ⁴ (approx 21.4 kbyte) to view full figure.]

⁵Click on icon to display Table 1.

Stochastic variability in the temperature data necessarily induces random fluctuations in the $\tilde{d}^{(1)}$ detection parameter, leading to the inevitable possibility of false positives. To assess properly the significance of episodes indicated by this detection parameter, we perform a nonparametric significance test in which we preserve the spatial correlation structure present in the data itself and model the temporal correlation structure in terms of AR(1) red noise. Red noise is an appropriate null hypothesis for the natural variability of the climate in the absence of specific “signals” or exogeneous forcings (see [Mann and Park, 1999](#), and discussion/references therein). To resample the temperature anomaly data in time without destroying its red-noise character, we modeled each grid-point time series as an autoregressive AR(1) process and obtained a residual “innovation” series. We permuted the (nominally) white-noise innovation series randomly in time using an identical resequencing for all grid points, implicitly retaining the baseline spatial correlation in the data. An ensemble of AR(1) series were then formed with these resequenced innovation series using the autoregressive parameters determined from the original data series. This algorithm obtains surrogate AR(1) temperature series that retain their original statistical persistence and spatial correlation structure. Confidence level estimates were obtained by applying the multiwavelet analysis to a large number of these surrogate instrumental temperature “datasets” and calculating relevant moments of the empirical distribution. A typical realization of this procedure is shown in [Figure 4](#), using the same conventions as in [Figure 3](#).

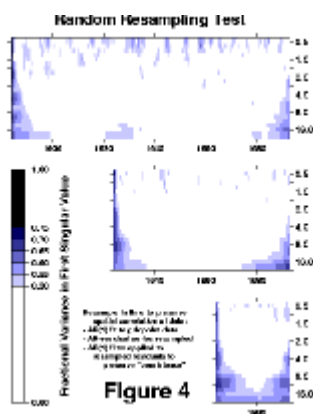


Figure 4. Time-frequency plot of $\tilde{d}^{(1)}$, the normalized first singular value of multiwavelet correlation matrices, in a resampled version of the temperature-anomaly dataset. Plotting conventions are similar to [Figure 3](#). Note the absence of significant episodes at interannual timescales. By contrast, serial correlation of the grid-point temperature anomaly series leads to nominally

significant values of $\bar{d}^{(1)}$. This suggests the danger of “false positives” when searching for significant surface-temperature episodes with oscillation timescale $T \cong 1$ year. [Click on icon ⁶ (approx 13.6 kbyte) to view full figure.]

Averaged over all timescales from 0.5 to 16 years, the bootstrap resampling scheme gives these confidence levels for nonrandom correlation: 90% for $\bar{d}^{(1)} > 0.52$, 95% for $\bar{d}^{(1)} > 0.535$, and 99% for $\bar{d}^{(1)} > 0.575$. These significance levels compare favorably with the guidelines for the frequency-independent analysis of Mann and Park ([Mann and Park, 1994](#)). The absence of variance concentration at interannual periods ($\cong 2$ years) in the resampling experiment ([Figure 4](#)) contrasts strongly with the data ([Figure 3](#)), for which prominent episodes are evident. However, because the correlation analysis at different timescales involves wavelets of different lengths, serial correlation (i.e., statistical persistence) in the temperature data leads to a frequency dependence in the null distribution of the \bar{d} parameter. Correlation estimates with shorter wavelets are subject to more false positives. This feature contrasts strongly with the frequency-independent null distribution of the detection parameter in the studies of Mann and Park ([Mann and Park, 1994](#); [Mann and Park, 1996](#); [Mann and Park, 1999](#)), in which a narrowband, frequency-localized (MTM-SVD) approach was used (a detailed discussion of this point is available in the work of [Mann and Park, 1999](#)). In the multiwavelet analysis, the frequency dependence of the null distribution is particularly evident at annual and shorter periods, which are within the persistence timescale of the temperature data itself ([Mann and Lees, 1996](#); [Mann and Park, 1999](#)). In contrast, the null distribution appears frequency independent at periods >1 year. The proper null distribution is obtained by averaging the parameter \bar{d} from the resampling experiments separately for each frequency. Rather than introducing this complication in representing the confidence levels of the detection parameter, however, we will simply adopt the criterion that a transient correlation represents a candidate “signal” only where $\bar{d}^{(1)} \cong 0.60$. This criterion is clearly conservative within the interannual timescales of interest in this study. Episodes at interannual timescales that meet this criterion typically coincide with well-known historical climate events, e.g., are centered on large historical El Niño years. We are skeptical of the significance of the “quasi-annual” episodes for which the above significance criterion is not appropriate. Even so, we report these for completeness in [Table 2](#).

⁷Click on icon to display Table 2.

4. ENSO-scale Variability

Prominent peaks in the detection parameter $d^{(1)}$ ([Figure 3](#)) appear at wavelet periods $T_c \sim 2.5\text{--}4$ years centered near 1920 and 1940. Other peaks occur at periods $2 < T_c < 4$ years, centered near 1974 and 1984. Somewhat weaker global interannual episodes are apparent

near 1900 and 1958. These peaks all represent particularly prominent oscillatory global temperature events within the classic ENSO period band. We also identify significant peaks in the decadal-to-interdecadal range including a streak in the 13- to 19-year range between 1940 and 1980 (with greatest prominence near 1960 at ~14-year period but showing a more persistent streak of variance near 16-year period) and a similar streak before 1920 centered near the 16-year period range, though it is blurred by boundary effects. The multiwavelet analysis complements, in this sense, the previous frequency-domain analyses of Mann and Park ([Mann and Park, 1994](#), [Mann and Park, 1996](#)), which support an intermittent interdecadal (16–18 year timescale) oscillatory climate signal with peak amplitude near 1900, the 1940s, and the 1970–1980s. In the multiwavelet analysis, degraded frequency-domain resolution makes it more difficult to distinguish this variability from secular trends in the data that show up as significant background variance near the 20-year period cutoff of [Figure 3](#). Note ([Table 1](#)) that for both interannual and decadal-scale episodes, a significant fraction of the temperature variations cancels in a global average. These episodes are thus associated with regional redistributions of heat at least as much as they are with changes in global mean temperatures.

It is of interest to examine the relationship between the character of the episodes identified above and the longer-term trends in global temperature during the past century. Of the two hemispheres, only the Northern Hemisphere (NH) provides a well-sampled record more than a century back in time (see [Jones and Briffa, 1992](#)). We thus use the NH series as a proxy for global temperature. The NH series is smoothed on timescales roughly corresponding to the secular cutoff in the multiwavelet analysis. The timing of the global ENSO-scale episodes bears an interesting relation to irregularities in the secular warming trend in the NH series ([Figure 5](#)). The secular increase is nonuniform, with rapid increases between 1920 and 1940 and after the early 1970s. Prominent global ENSO episodes in the multiwavelet analysis coincide with the endpoints of these intervals. This encourages the hypothesis (e.g., [Graham, 1994](#), [Graham, 1995](#); [Trenberth and Hoar, 1996](#), [Cane et al., 1997](#)) that tropical climate dynamics governs the pace of global temperature increase, whether it is natural or anthropogenic, most likely by modulating heat exchange between atmosphere and ocean. The early 1980s ENSO episode does not fit neatly into this pattern, however. Indeed, as noted below, the 1980s episodes were unusual in a number of ways.

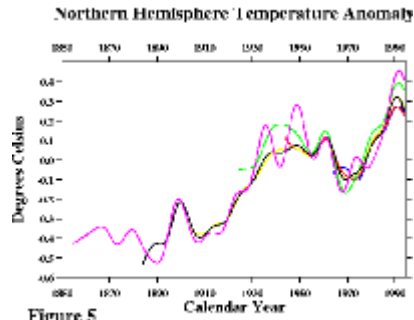


Figure 5

Figure 5. NH mean temperature anomalies based on the fixed grids of all available global land air and sea surface temperature data ([Jones and Briffa, 1992](#)) back to 1854, 1884, 1904, 1924, 1944, and 1964. Area-weighted averages of gridpoints were lowpassed at 12-year period with a simple sinc-function filter with a Lanczos convergence factor ([Bloomfield, 1976](#)). Aside from 1930 to 1950, the different averages agree well in trend. The largest departure in the 1930–1950 interval involves decadal-scale oscillations in the averaged 1854–1993 dataset. This longest dataset is also the sparsest and is relatively dominated by grid points in the North Atlantic region, a locus of quasi-decadal climate variability ([Mann and Park, 1994](#); [Mann and Park, 1996](#); [Mehta and Delworth, 1995](#)). Note the steepest increases in NH mean temperature are confined to the intervals 1920–1940 and 1975–present. The decrease in temperature in the early 1990s is not a filtering artifact and likely represents the cooling influence of 1991 Pinatubo eruption. [Click on icon ⁸ (approx 12.0 kbyte) to view full figure.]

Using the methods described in [section 2](#), we can reconstruct the spatiotemporal pattern of the 1980s interannual signal. In a time-frequency neighborhood centered on 1984 and 2.8-year period, the principal eigenvector describes a fraction $\tilde{d} = 70.0\%$ of the multivariate data variance (standardized and area-weighted) in the 1570-grid point 1965–1993 temperature dataset. The temperature signal is not a simple sinusoidal oscillation, displaying a time-limited and broadband character ([Figure 6](#)). The wavelet period (2.8 years) locks onto the dominant timescale of the El Niño/La Niña alternation. However, the recurrence interval between large El Niño events, 4 years in this case, can also be used to define an ENSO periodicity (e.g., [Quinn and Neal, 1992](#)). Indeed, both of these interannual timescales are evident on frequency-domain analyses of 20th century climate data ([Mann and Park, 1994](#); [Mann and Park, 1996](#)) and appear to have slightly drifted during this century ([Mann and Park, 1996](#)).

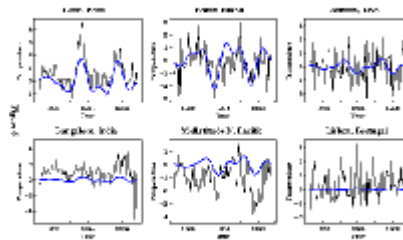


Figure 6. Comparisons of the raw temperature anomaly data (in °C) with wavelet signal reconstructions for the 1980s global ENSO episode. Note that the wavelet reconstruction has zero mean and so cannot represent constant shifts in baseline temperature. The ability of the Slepian wavelets to incorporate phase shifts is evident in the delay of the Atlanta and mid-Pacific temperature cycles relative to Lima, Peru. Shortcomings in the wavelet reconstruction can be seen in the disparate amplitudes of the 1983 and 1987 El Niño events recorded at the Lima and the North Pacific grid points and the weak correlation with interannual variability at the Lisbon grid point. [Click on icon ⁹ (approx 14.4 kbyte) to view full figure.]

The pattern in amplitude and phase of the 1980s temperature signal is shown in [Figure 7](#). High-amplitude temperature variations are observed in the eastern equatorial Pacific (the core region of El Niño) followed at a roughly 1-year lag (120° phase delay) by strong warming in the polar regions of both hemispheres. The signal exhibits large temperature variations in the central North Pacific and extratropical North America, relatively robust regions of extratropical influence or “teleconnection” of ENSO (e.g., [Halpert and Ropelewski, 1992](#)). Large responses are also observed in central and north Asia. Amplitudes of the signal for selected regions are shown in [Figure 8](#). The spatial pattern of greatest amplitude is similar, but equivalent, to the pattern of where the signal “fits” the data best, in terms of the fraction of variance in the raw data described by the reconstructed signal. The signal most closely describes the observed temperature variations in the tropical oceanic regions, midlatitude coastal regions of North America, boreal Canada and Siberia, China, and the midlatitude North Pacific. The signal describes least well the variability in Europe, Patagonia, the Gulf of Alaska, and the Sargasso Sea; in each case, a region where the signal is quite weak. The global average of this pattern has peak-to-peak variation $T_{GLB} = 0.21^{\circ}\text{C}$, but individual grid points vary by as much as $\Delta T = 3.6^{\circ}\text{C}$ ([Table 1](#)).

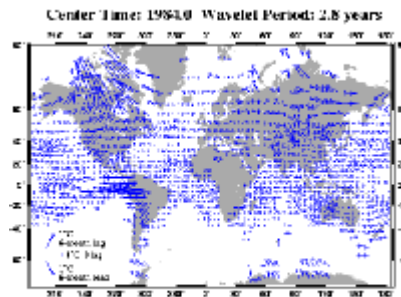


Figure 7

Figure 7. Spatial pattern associated with the wavelet signal reconstruction of the 1980s global ENSO episode centered near 2.8-year period. The length of the arrows indicates the amplitude of temperature variations. Peak-to-peak temperature variation for the gridpoint containing Lima, Peru (12.5°S, 77.5°W) is 2.5°C. Arrow direction indicates the temporal lag at each grid point, relative to the gridpoint containing Bangalore, India. Zero-phase points toward “3 o'clock,” and lag increases counterclockwise. Clockwise arrow rotation represents lead relative to zero phase. The 360° corresponds to the $T_c \sim 2.8$ -year wavelet period. [Click on icon ¹⁰ (approx 26.9 kbyte) to view full figure.]

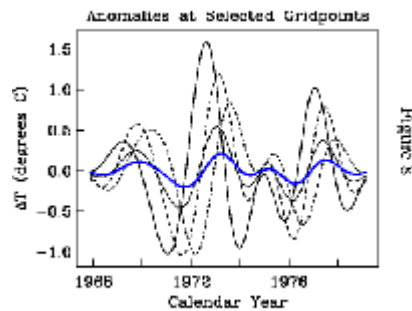


Figure 8. Wavelet signal reconstructions (temperature anomalies in °C) for 1970s global ENSO episode. Selected grid points include Lima, Peru (fine solid line); Bangalore, India (fine dash); Tashkent, Uzbekistan (medium dash); and Nome, Alaska (large dash). The thick blue solid line is the area-weighted global average of all grid points for this wavelet reconstruction. [Click on icon ¹¹ (approx 11.0 kbyte) to view full figure.]

Earlier global ENSO episodes detected in the analysis exhibit similar behavior in the tropics, but differ in their midlatitude and high-latitude patterns of influence, that is, the inferred teleconnections. In a time-frequency neighborhood centered on 1973.5 and 2.8-year period, the principal eigenvector describes an impressive $\bar{d} = 74.2\%$ of the data variance in

the 1570-grid point 1964–1993 dataset (greater, the reader will note, than the well-known 1980s signal). Relative to the 1980s pattern, the 1970s signal exhibits higher-amplitude variations in the continental United States and weaker amplitudes in boreal regions. The signal is stronger in the Gulf of Alaska, Kazakhstan, and Patagonia. The reconstruction of the temporal signal ([Figure 8](#)) is characterized by a 2.6°C peak-to-peak 1971–1973 La Niña/El Niño sequence in Peru (i.e., cooling, then warming), followed by a smaller (~1.5°C) El Niño event in 1977. The South American coastal signal is lagged 4 months by weaker variations in the Indian Ocean region. As with the 1980s pattern, the global spatial average of the signal peaks 1–2 months after maximum amplitude in the Indian Ocean region, with a peak-to-peak global temperature variation ([Table 1](#)) $T_{GLB}=0.41^{\circ}\text{C}$, twice as large as the 1980s episode.

[Figure 9](#) illustrates the global pattern of the signal with a sequence of snapshots. The reader will note classic peak El Niño conditions during winter 1972/1973 in the snapshot sequence.

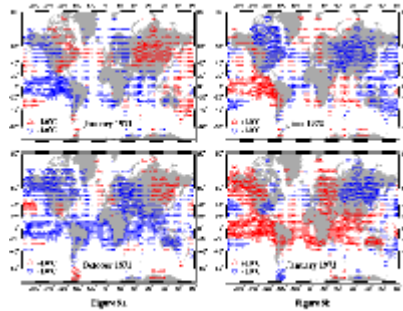


Figure 9. Spatial snapshots from the wavelet signal reconstruction of the 1970s global ENSO episode, centered at 1973.5 and 2.8-year period. The La Niña and El Niño conditions of January 1971 and January 1973 are accompanied by a marked east-west asymmetry in temperature anomalies across North America and, with slightly different phase, Eurasia. A similar asymmetry is evident between Australia and New Zealand, in the midsummer Southern Hemisphere. [Click on icon ¹² (approx 35.9 kbyte) to view full figure.]

In a time-frequency neighborhood centered on 1940 and 2.8-year period, the principal eigenvector describes a fraction $\bar{d} = 63.4\%$ of the normalized temperature variance in the 663-grid point 1924–1993 dataset. At midlatitude and high latitudes, grid points in Europe, Kazakhstan, East Asia, Alaska, southeast Australia, and southeast Africa are represented best. The wavelet-reconstruction of this variability is characterized by an oscillatory pattern that increases in amplitude and frequency from 1935 to 1945. This temporal signal is shown for selected regions in [Figure 10](#). Tropical variability is modest relative to episodes in the 1970s and 1980s, with the Lima grid point's peak-to-peak $\Delta T \sim 0.9^{\circ}\text{C}$. Instead, large, spatially coherent temperature swings characterize much of midlatitude Eurasia, peaking in excess of 2.5°C within Russia. The area-weighted global average of this pattern nearly

vanishes, with peak-to-peak $T_{GLB} = 0.05^{\circ}\text{C}$. In snapshots of the reconstructed signal pattern (Figure 11), Peruvian anomalies are largely opposite to those in equatorial Asia and east Africa. This pattern is unusual for recent ENSO variability, as discussed in more detail below.

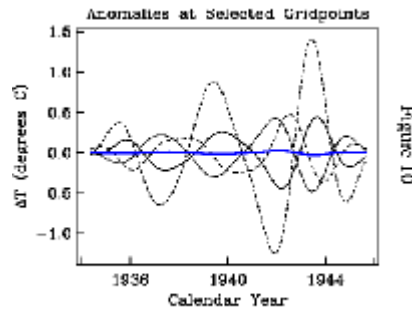


Figure 10. Wavelet signal reconstruction of temperature variations at different grid points (in $^{\circ}\text{C}$) for the global ENSO episode centered near 1940 and 2.8-year period. Selected grid points include Lima, Peru (fine solid line); Bangalore, India (fine dash); Moscow (medium dash); and Melbourne, Australia (large dash). The thick solid line is the area-weighted global average of all grid points for this wavelet reconstruction. [Click on icon ¹³ (approx 8.8 kbyte) to view full figure.]

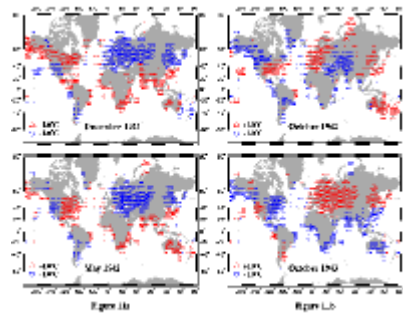


Figure 11. Spatial snapshots from the wavelet signal reconstruction of the global ENSO episode centered at 1940 and 2.8-year period. Temperature patterns are consistent with a North Atlantic Oscillation (NAO) anomaly in one interval of the cycle (see “October 1942”), with temperature anomalies in Greenland opposite in sign to anomalies in Europe and offshore the Canadian Maritimes. At other points in the cycle, however, very broad spatial coherence across continents is evident. [Click on icon ¹⁴ (approx 30.0 kbyte) to view full figure.]

In a time-frequency neighborhood centered on 1920 and 4.0-year period, the first singular-vector pair can explain 67.0% of the area-weighted temperature variability in the

500-grid point 1904–1993 dataset. At midlatitude and high latitudes, grid points in northwestern North America, Greenland/Iceland, Patagonia, and eastern Australia are represented best. Peruvian temperature anomalies lead Asian equatorial locations, particularly India, by roughly 1 year ($\sim 90^\circ$ for $T_c = 4.0$ years). The signal is characterized by an plus-minus-plus pulse of temperature at the Lima grid point with $\Delta T = 1.8^\circ\text{C}$, followed by weak fluctuation in the 1920s (Figure 12). The area-weighted global average of the wavelet reconstruction has peak-to-peak amplitude 0.48°C . In snapshots from the late 1910s (Figure 13), a strong North-Atlantic Oscillation (NAO) is evident. Grid points in coastal Peru and coastal Angola lead and lag, respectively, the temperature signal at nearly all other tropical grid points by roughly 1 year.

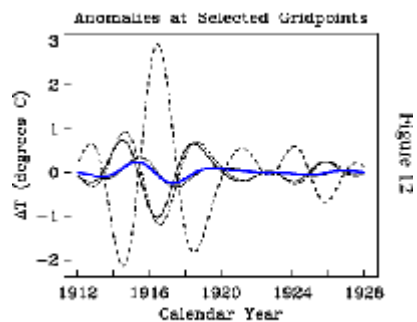


Figure 12. Wavelet signal reconstruction of temperature variations at different grid points (in $^\circ\text{C}$) for the global ENSO episode centered near 1920 and 4.0-year period (i.e., ENSO-scale). Selected grid points include Lima, Peru (fine solid line); Bangalore, India (fine dash); Billings, Montana (medium dash); and Godthaab, Greenland (large dash). The thick solid line is the area-weighted global average of all grid points for this wavelet reconstruction. [Click on icon ¹⁵ (approx 8.45 kbyte) to view full figure.]

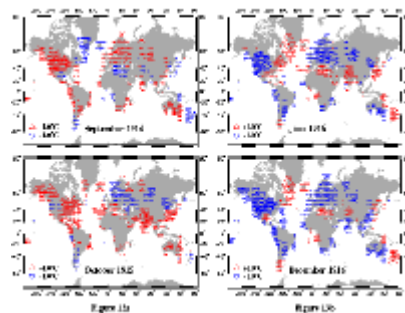


Figure 13. Spatial snapshots from the wavelet signal reconstruction of the global ENSO episode centered near 1920 and 4.0-year period. Grid points in coastal

Peru and coastal Angola appear to lead and lag, respectively, the temperature signal at nearly all other tropical gridpoints by roughly 1 year. Large fluctuations (2° – 5°C) in the Pacific Northwest and Greenland oppose those in coastal Peru. Eastern Australia and New Zealand have large anomalies, but with opposing signs. [Click on icon ¹⁶ (approx 29.1 kbyte) to view full figure.]

The global ENSO episode centered near 1957 (not shown) is associated with the 1957 El Niño that raised monthly temperatures in the Lima, Peru grid point by 4°C . The correlated episode centered on 1900 and 3.4-year period explains 62.9% of the area-weighted temperature variability in the 368-grid point 1884–1993 dataset. Although tropical grid points are sparse in this dataset, particularly in the eastern tropical Pacific, coherent low-latitude temperature changes finger ENSO as a principal influence on the pattern.

ENSO variability at interdecadal timescales is also evident in the wavelet analysis. In a time-frequency neighborhood centered on 1960 and 13.5-year period corresponding to the maximal correlation peak within a broader interdecadal streak of high correlation between 1940 and 1980, the first singular-vector pair can explain 64.6% of the area-weighted temperature variability in the 668-grid point 1924–1993 dataset. In the pattern, in-phase tropical warmth and coolness are evident, coherent with similar temperature variations around the northern Pacific. Temperature fluctuations of opposite sign occur over Europe, so that cancellation in the average leads to a global $T_{\text{GLB}} = 0.21^{\circ}$. At longer wavelet period the wavelet analysis should become more equivalent to techniques based directly on the Fourier transform, so it is not surprising that this temperature signal resembles the interdecadal (16- to 18-year timescale) signal identified by Mann and Park ([Mann and Park, 1993](#), [Mann and Park, 1994](#) [Mann and Park, 1996](#)). The proximity in frequency of decadal and interdecadal climate signals, however, weakens the utility of wavelet-based analysis. For instance, this episode explains decadal-scale temperature variance well at low latitudes and in the North Pacific but less well in the North Atlantic region and Europe, where significant quasi-decadal ($T \sim 10$ – 12 years) variability appears that seems unrelated to ENSO (e.g., [Deser and Blackmon, 1993](#); [Mann and Park, 1994](#); [Mann and Park, 1996](#); [Mehta and Delworth, 1995](#)).

When compared with grid-point data series, the relationship of the interdecadal cycle to the spacing between the major ENSO episodes of 1941/1942, 1957/1958, and 1972–1987 is clear ([Figure 14](#)). Note also that peak cycle amplitudes near 1940, 1960, and 1980 correspond to positive fluctuations in the hemispheric average temperature in [Figure 5](#), the last as an upward ripple in the 1975–present warming interval. There appears to be a relationship ([Figure 3b](#)) between the interdecadal periods of peak tropical warmth and the timing of high-amplitude interannual episodes. This observation supports the hypothesis that interdecadal climate changes, possibility associated with or enhanced by North Pacific extratropical coupled ocean-atmosphere dynamics ([Latif and Barnett, 1994](#)) may influence ENSO in the tropical Pacific (see the discussion by [Mann and Park, \(1996\)](#)).

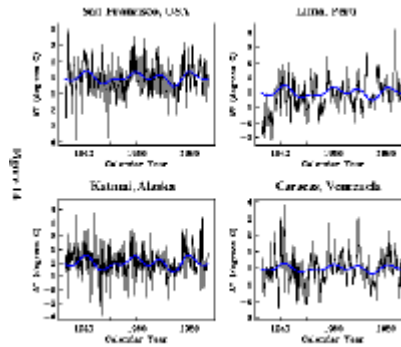


Figure 14. Comparisons of raw temperature anomaly data (in °C) with wavelet signal reconstructions from the interdecadal (~15-year timescale) signal between 1933 and 1987. Note the local maxima of the interdecadal signal that coincide with the 1940 and 1957 interannual episodes, as well as the steep increase leading into the warmth of the early 1980s. [Click on icon ¹⁷ (approx 17.7 kbyte) to view full figure.]

The relative timing of temperature anomalies in the eastern tropical Pacific (e.g., the relative phases of Peruvian grid points) during the 1920s and 1940s global ENSO episodes differ significantly from that observed in the better sampled episodes of the 1970s and 1980s. This suggests a departure from the standard ENSO pattern during these episodes, though potential data biases must be considered. Jones and Briffa ([Jones and Briffa, 1992](#)), for example, identify several sources of bias in the instrumental sea surface temperature records specific to the war years of the early 1940s. These are due to changes in bucket-collection measurements of sea surface temperatures and a migration of weather stations away from city centers starting in the 1940s. Stepwise shifts in baseline temperatures, induced by biases of these types, could lead to “Gibbs-effect” ringing in bandpassed correlation estimates, similar to contamination at the endpoints of the analyzed time intervals. However, comparison of temperature anomalies from selected grid points with their wavelet reconstructions does not suggest effects of this kind ([Figure 15](#)). The Southern Oscillation Index (SOI) is positive in 1917 and negative in 1919 and 1941, matching coeval cooling (La Niña) and warming (El Niño), respectively, at eastern equatorial Pacific grid points.

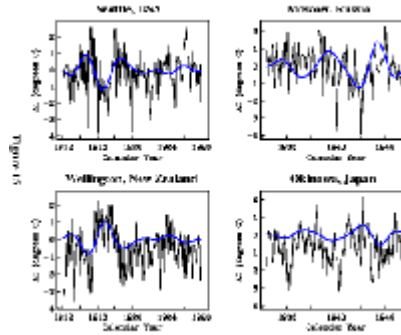


Figure 15. Comparisons of raw temperature anomaly data (in °C) with wavelet signal reconstructions for the global ENSO episodes centered near 1920 (e.g., [Figure 11](#)) and 1940 (e.g., [Figure 13](#)). Note that the wavelet signal reconstruction has zero mean and so cannot represent shifts in baseline temperature. Historical note: extreme cold in the winter of 1941/1942 was a contributing factor in Hitler's failure to seize Moscow in the World War II. [Click on icon ¹⁸ (approx 17.4 kbyte) to view full figure.]

Shifts in baseline temperature are evident in some locations but are difficult to ascribe to data biases. [Figure 16](#) compares data and wavelet reconstructions for grid points containing Darwin (Australia), Lima (Peru), and Cali (Columbia). The Lima grid point suffers abrupt cooling in 1920 and abrupt warming at the end of 1937. Aside from the El Niños of 1925 (termed “very strong” by Quinn and Neal ([Quinn and Neal, 1992](#))), 1930 and 1932, temperatures are depressed by 1°–2°C through most of the intervening period. Similar behavior is evident at grid points adjacent to Lima but is not evident in the Cali grid point, closer to the equator. Unless a large transient bias near Peru has contaminated temperature data in this interval, an unusual persistence of coastal upwelling offshore central Peru is indicated. For the 1920 episode, the wavelet reconstruction fades to low amplitude as temperatures dip in the Lima grid point, so the shift in baseline temperature has little effect on it. For the 1940 episode, the wavelet reconstruction grows in amplitude gradually, straddling the temperature jump. As a result, its negative slope in 1940–1942 coincides with almost uniformly warm, but weakening, El Niño conditions. Comparison with the Cali grid point confirms that these adjacent portions of the South American coast experienced opposing temperature-anomaly trends in the early 1940s. Because the Slepian wavelets underlying our multivariate signal detection method are optimally band-limited, this ENSO-scale quasi-cycle can be identified independent of the stepwise jump just before 1938.

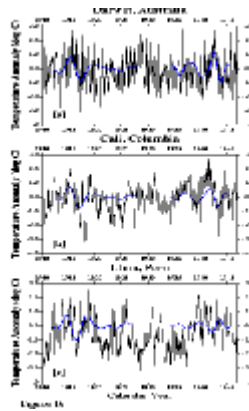


Figure 16. Wavelet reconstructions of the 1920 and 1940 correlated episodes, plotted atop monthly temperature anomaly data at three low-latitude grid points, containing (a) Darwin, Australia; (b) Cali, Columbia; and (c) Lima, Peru. Note the depression in temperatures in the Lima grid point during the 1920–1940 interval. [Click on icon ¹⁹ (approx 19.6 kbyte) to view full figure.]

5. Summary

Because this study is an empirical reconnaissance of historical climate data, not a test of a specific dynamical hypothesis, conclusions drawn from it must be tentative. Nevertheless, we can make several observations on the basis of our analysis and hypothesize a scenario that may connect them. The first of the observations is quite unsurprising. The others encourage further investigation, either with other datasets or with dynamical models.

1. *Global-scale ENSO variability, with root-mean-square (rms) grid-point temperature fluctuations $\Delta T = 0.6^{\circ}$ – 1.1°C , seems to be well described as an episodic oscillation with band-limited character.* All interannual correlated temperature episodes that explain 60% or more of bandpassed normalized temperature-anomaly variance involve one or more El Niño events in the eastern equatorial Pacific. Although these episodes share common timescales, they display distinct time histories and spatial patterns. Details of ENSO teleconnections may depend on an evolving “base state” of the global circulation. This may explain why some pairs of El Niño events (e.g., the pair for 1972 and 1976/1977 and the pair for 1982/1983 and 1986/1987) are sufficiently similar to appear as one correlated episode but differ significantly from ENSO variability in other decades. The ENSO-like 16- to 18-year temperature cycle, found also in earlier studies, emerges from the background variability as a “pacemaker” of the major ENSO episodes since 1935, with largely in-phase temperature changes throughout the tropics and North Pacific region.

2. *The 1920–1940 interval of increasing NH mean temperatures was bracketed by two unusual globally correlated ENSO episodes.* Relative to the well-studied ENSO patterns of the 1970s and 1980s, the spatial patterns of the episodes centered on 1920 and 1940 exhibit

unusually strong midlatitude and high-latitude teleconnections. Southern Peru and Angola exhibit phase shifts relative to the equatorial zone that are much larger than in subsequent ENSO-scale episodes, where phase leads of only a few months are more typical. The temporal evolution of these episodes is also unusual. The 1920-centered episode suggests an abrupt cessation of globally teleconnected anomalies at the end of 1919, coincident with a $1^{\circ}\text{--}2^{\circ}\text{C}$ drop in baseline temperatures in the grid points surrounding Lima, Peru. In contrast, the 1940-centered episode slides upward in both amplitude and frequency from a starting point in the mid-1930s, culminating in the 1941/1942 El Niño episode. This crescendo of temperature variability straddles the recovery at the end of 1937 of the baseline temperature level in the grid points surrounding Lima. A connection between the timing of these episodes, the rapid 0.5°C global temperature change in 1920–1940, and upwelling along coastal Peru may be hypothesized.

The decades between 1920 and 1940 also exhibit unusual behavior in historical records of tropical atmospheric sea-level pressure. Some authors have speculated that a significant change in atmosphere-ocean circulation occurred during this interval. The ~ 20 -year interval of NH mean warming is characterized by a deficit of interannual variability in various ENSO indices ([Trenberth and Shea, 1987](#); [Elliot and Angell, 1988](#); [Gu and Philander, 1995](#); [Wang and Wang, 1996](#)). Despite muted SOI variability, low-latitude South America suffered a “very strong” El Niño in 1925 ([Quinn and Neal, 1992](#)) that was clearly expressed in tree-ring ([Lough, 1992](#); [D'Arrigo and Jacoby, 1990](#)) and flood ([Cayan and Webb, 1992](#)) records from the western United States. The detection parameter $\tilde{d}^{(1)}$ in [Figure 3](#) exhibits a weak peak at $T \cong 2$ years in the late 1920s, but the global expression of the 1925 El Niño was not strong enough to be identified as an “episode” in the temperature anomaly dataset, according to our criteria. [Trenberth and Shea \(1987\)](#) point out that the pattern of correlated atmospheric pressure variations associated with the Southern Oscillation after 1940 do not hold when the time interval is extended back to the early 20th century. [Elliot and Angell \(1988\)](#) suggest that pressure differences between Darwin and the eastern Pacific are a more reliable measure of the Southern Oscillation before 1920 than pressure differences between Darwin and Tahiti, in the central Pacific, which is the preferred choice after 1940 (e.g., [Trenberth, 1984](#)). A shift in the relative amplitudes of ENSO-related interannual temperature and SLP variability in the subtropical north Pacific across the 1920–1940 interval was also noted by [Mann and Park \(1996\)](#). This may reflect a shift in ENSO dynamics associated with the 1920–1940 secular warming.

3. The 1920–1940 and 1975–present intervals of increasing NH mean temperatures were preceded by ENSO episodes associated with large swings in global-mean temperature. These swings of $T_{\text{GLB}} > 0.4^{\circ}\text{C}$ are the largest among the correlated interannual episodes ([Table 1](#)). In contrast, the correlated episode centered on 1940, which concludes the 1920–1940 temperature rise, has area-weighted $T_{\text{GLB}} = 0.05^{\circ}\text{C}$, smallest among interannual episodes. It is too soon to tell whether NH warming since 1975 has terminated or whether it

will terminate in a sequence of large-amplitude ENSO-related interannual oscillatory behavior. Like the strong 1925 ENSO event, the 1982–1987 ENSO episode is relatively weakly correlated with interannual temperature anomalies in the extratropics, aside from grid points in northern Canada. These parallels between the warming intervals are suggestive, but there are distinctions as well. Strong extratropical teleconnections and unusual relationships in the eastern tropical Pacific (e.g., among the Peruvian temperature grid points) are evident in the 1920 episode, but not the episode in the 1970s.

A possible link between the intervals of warming is an increase in extreme meteorological conditions, such as droughts and floods. The historical record of such events is often (by nature) anecdotal; e.g., Borisenkov ([Borisenkov, 1992](#)) notes that Russia suffered an increased incidence of extreme winters, both warm and cold, in the two decades after 1925. In an attempt to standardize such comparisons, Karl et al. ([Karl et al., 1995](#)) developed an index of extreme climate events, restricted to the United States; see also Kerr ([Kerr, 1995](#)). This index peaks both in the 1930s and the 1980s. Increases in this index in the 1980s were interpreted by Karl et al. ([Karl et al., 1995](#)) as a possible indicator of anthropogenic greenhouse warming. Our multiwavelet analysis suggests that such decadal changes might be strongly influenced by changes in ENSO teleconnections during the two ~20-year intervals of greatest secular warming. Greenhouse warming in this sense might be an indirect, rather than direct, cause of changes in the frequency and intensity of climatic extremes. Such extremes may become more numerous during any significant transition in the global climate, regardless of the cause.

4. *Prominent “quasi-annual” global episodes in the 20th century occur no more often than expected from Monte Carlo simulations of temperature anomaly data that possesses the stochastic temporal and spatial correlation structure estimated from the grid-point surface temperature dataset.* [Table 2](#) describes the vital statistics of the most prominent “correlated episodes” with oscillation period $T \sim 0.5\text{--}1.0$ year. Most involve a succession of similar wintertime temperature anomaly patterns, with rms fluctuations $\Delta T \cong 1.5^\circ\text{--}2.0^\circ\text{C}$, and global-mean fluctuations $\lesssim 188 > 0.4^\circ\text{C}$. Many short-period episodes appear to coincide with large volcanic eruptions, which are known to depress average surface temperature by as much as 0.5° for a year or more ([Groisman, 1992](#); [Robock and Mao, 1992](#); [Kelly et al., 1996](#)). After reconstructing their time histories, however, the short-term episodes identified by wavelet correlation usually precede the largest 20th century volcanic eruptions (e.g., [Simkin and Siebert, 1994](#)), rather than follow them. The rms grid-point temperature fluctuations in [Table 2](#) exceed greatly the expected $0.2^\circ\text{--}0.5^\circ\text{C}$ volcanic cooling signal, suggesting that natural temperature variability is too large for volcanic cooling (in the 20th century) to emerge as a significant signal in the multiwavelet analysis.

6. Discussion

The coherent spatiotemporal patterns of temperature variation revealed by the multiwavelet analysis may have more than one possible explanation. Only a handful of highly significant interannual episodes are isolated in the temperature anomaly dataset, so any hypothesized relationship between them will not be strongly constrained. Nevertheless, the coincidence of significant ENSO episodes with the irregularities in the upward trend of average temperature deserves attention, suggesting possible dynamical linkages that could be investigated in coupled ocean-atmosphere model experiments. We propose a hypothetical scenario to frame further investigation.

Secular change in the heat budget of the climate system need not alter the temperatures of each system component at the same rate. The global temperature dataset analyzed here monitors temperature in the lower atmosphere and at the sea surface, but not in the subsurface ocean. Heat exchange between the atmosphere/sea-surface and the subsurface ocean is an essential part of the global ENSO phenomenon. If the climate system has gradually warmed in the 20th century owing to increasing anthropogenic CO₂ (or perhaps, a combination of anthropogenic and natural, e.g., solar, forcing), the irregular rise in observed average atmosphere/sea-surface temperature could be due to long-term variations in the exchange of heat with the ocean. The timing and characteristics of the 20th century ENSO episodes listed in [Table 1](#) can be used to argue for a scenario by which this exchange occurs. In the early and middle decades of the 20th century, successive ENSO episodes are associated with increasing peak-to-peak projection onto global and hemispheric mean temperature, up to the point where secular warming commences, approximately at 1920 and 1975 ([Figure 17](#)). One interpretation of this behavior is that excess warmth in the climate system is initially stored in the tropical ocean and seeks release to the atmosphere via ENSO, the most prominent natural instability of the coupled atmosphere-ocean system whereby heat exchange with the ocean occurs. A simple increase in tropical SST would transmit heat readily to the lower atmosphere via convective dynamics, so an oceanic heat-storage “flywheel” would more likely take the form of a thickened upper ocean layer.

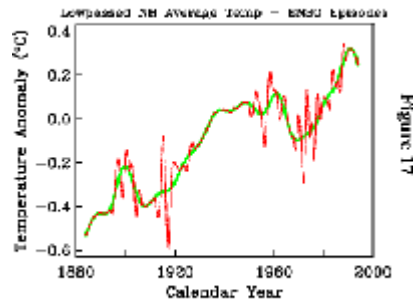


Figure 17. Superposition of the NH mean of the interannual ENSO episodes onto the smoothed NH mean temperature record, based on all grid points with

continuous monthly coverage back to 1884. In the decades prior to both 1920 and 1980, increasingly large swings in NH mean temperature are associated with global ENSO episodes. [[Click on icon ²⁰ \(approx 11.2 kbyte\) to view full figure.](#)]

This seemingly simple scenario is nonetheless difficult to test with current theoretical models of ENSO, owing to the lack of a truly satisfactory representation of El Niño variability in the contemporary global coupled ocean-atmosphere models used to assess anthropogenic climate-change scenarios. The most detailed measurements of ENSO behavior have been taken in the past few decades, largely since 1975 in the current interval of secular warming. When viewed over the entire 20th century with the available global temperature data, however, episodes of globally coherent ENSO variability appear as largely zero-sum heat exchanges. Theoretical models embracing the “delayed oscillator” mechanism of ENSO dynamics provide some justification for this observation. Positive SST anomalies in the tropical Pacific associated with a warm (El Niño) event excite combinations of oceanic Rossby and Kelvin waves that erode anomalously warm conditions in the central Pacific and plunge the region into anomalously cool SST ([Kessler and McPhaden, 1995](#); [Chelton and Schlax, 1996](#); [Battisti, 1990](#)). In this “La Niña” portion of the cycle, the shoaling upper ocean layer draws heat back from the lower atmosphere, diminishing the net exchange of heat. Using a high-resolution tropical model, Cane et al. ([Cane et al., 1997](#)) argue that enhanced “La Niña” conditions, in which the zonal SST gradient strengthens in the tropical Pacific, occur, seemingly paradoxically, as a direct response to enhanced-greenhouse radiative heating, due to the feedback mechanisms originally identified by Bjerknes ([Bjerknes, 1969](#)). Cane et al. ([Cane et al., 1997](#)) argued that this mechanism has largely offset the 20th century warming that otherwise might have been expected in the tropical Eastern Pacific due to enhanced greenhouse radiative forcing, and that this effect has, further, diminished the 20th century warming of the globe on the whole. This picture clashes, however, with the paradigm that emerges from coupled model experiments of ENSO dynamics under an anthropogenic forcing scenario. These favor the alternate view of persistent El Niño conditions as a major symptom of enhanced greenhouse warming (e.g., [Meehl and Washington, 1996](#); [Knutson et al., 1997](#)). This paradigm is seemingly endorsed by the “perpetual” El Niño of the early 1990s (e.g., [Graham, 1995](#); [Trenberth and Hoar, 1996](#); [Goddard and Graham, 1998](#)).

We speculate that both paradigms for the relationship between ENSO and anthropogenic warming may be valid but over distinct time intervals in the 20th century. In order for El Niño conditions to foster, rather than inhibit, secular atmospheric warming, the La Niña-like feedback argued for by Cane et al. ([Cane et al., 1997](#)) would need to weaken or be offset by other mechanisms. Secular change in ENSO dynamics could occur via changes in its boundary conditions, e.g., via an upper ocean layer that thickens over time. Gu and Philander ([Gu and Philander, 1997](#)) hypothesize that the tropical upper ocean layer thickens at its base if warm extratropical waters descend along isopycnal surfaces. Since it may take decades for tropical SST anomalies to migrate to midlatitude isopycnal outcrops, this mechanism can, at least in a suitably simplified model, sustain interdecadal oscillations (see [Gu and Philander,](#)

1997). Hypothetically, this mechanism could also lead to secular changes, tending to offset the Cane et al. (Cane et al., 1997) negative feedback; although Cane et al. (Cane et al., 1997) argue against the latter based on ocean GCM experiments. In the scenario where subduction of greenhouse-warmed extratropical surface waters thickens the tropical upper ocean layer over time, we might imagine that secular greenhouse warming disrupts ENSO feedbacks through a change in the dynamical response of the tropical upper ocean layer. With Bjerknes feedbacks absent or weak, local thermodynamic considerations could dominate the response to anthropogenic forcing (see, e.g., the discussion by Cane et al. (Cane et al., 1997)), and the tropical Pacific could suffer persistent El Niño conditions, quiescent interannual variability, and a net heat exchange from ocean to lower atmosphere. The climate state evolves until the ocean/atmosphere heat partition reaches a new quasi-equilibrium. Persistent El Niño conditions in the early 1990s (e.g., Graham, 1995) may reflect this process, as Kessler and McPhaden (Kessler and McPhaden, 1995) note that observed Rossby and Kelvin waves failed to induce the “delayed oscillator” effect predicted by numerical models, and Goddard and Graham (Goddard and Graham, 1998) noted an unusual vertical thermal structure to the early/mid 1990s El Niños. As a corollary, if teleconnections are weak, the geographic reach of even “very strong” El Niño events, like that of 1925, becomes more limited. The 1980s correlated ENSO episode, despite its worldwide scientific and public attention, displays weaker correlation between tropical and extratropical temperature anomalies than does the 1940s episode.

In this speculative scenario, an increasing heat imbalance between atmosphere and ocean would be reflected by an increasing projection T_{GLB} of ENSO variability onto global-mean temperature. In the 20th century, peak-to-peak T_{GLB} seems limited by 0.45°C , roughly equivalent to the secular temperature increase in 1920–1940. After secular warming relieves the atmosphere-ocean heat imbalance, the upper ocean layer returns to its more normal state and the Bjerknes feedbacks resume as the tropical ocean settles into a new quasi-equilibrium state. With the Bjerknes feedbacks operational, secular warming is ameliorated or halted by the negative feedbacks described by Cane et al. (Cane et al., 1997), the delayed oscillator mechanism is active, and high-amplitude interannual episodes are observed. Evidence for just such a relationship between secular and interannual variability is suggested by Figure 17. A quasi-equilibrium interval is suggested by nearly constant NH mean temperatures from 1940 to 1975. The weak global-mean temperature projection $T_{\text{GLB}} = 0.05^{\circ}\text{C}$ of the 1940s ENSO episode, which inaugurates this interval of stable temperature, is consistent with the notion of a rough heat balance between atmosphere and ocean after the 1920–1940 warming interval. Evidence for a change in the “centers of action” in the Southern Oscillation Index after 1940 (e.g., Elliot and Angell, 1988) is also consistent with the establishment of a new dynamical regime in the tropical Pacific at that time.

It is germane to ask if this study can shed any light on whether the 20th century increase in global temperature is anthropogenic or the result of natural variability. Natural variability

cannot be rejected out of hand as a contributing factor, because periods of exceptional ENSO variability are also suspected to correlate with large pre-industrial climate variations ([Quinn and Neal, 1992](#)). Exceptional variability can also be found in both long ENSO-proxy records ([Dunbar et al., 1994](#)) and in low-resolution coupled ocean-atmosphere model simulations ([Knutson et al., 1997](#)). On the other hand, we have identified behavior in the instrumental temperature record that motivates a scenario of how hemispheric temperatures might increase irregularly in response to a steady increase in radiative forcing. This scenario suggests that if atmosphere and ocean reequilibrate after the post-1975 interval of secular atmospheric warming, global temperatures might level off for a few decades, similar to the 1940–1975 interval. Any such respite would likely be followed, however, by another interval of rapid warming. One can imagine that such a pause in the warming trend would complicate the incontrovertible detection of anthropogenic climate forcing and, moreover, any international governmental efforts to reduce greenhouse gas emissions. The irregularity of warming during the 20th century has been cited as a reason to doubt a causal connection with more monotonically increasing greenhouse gas concentrations (e.g., [Balling, 1992](#)). Further study is needed to determine how ENSO and its large-scale patterns of influence might change character in response to changing boundary conditions associated with greenhouse warming or other external forcing of climate and what timescales of response might be expected for such changes.

Acknowledgments. Aime Fournier and Barry Saltzman made several useful comments on the manuscript. This work was supported in part by the National Science Foundation Hydrological Sciences program (grant EAR-9720134). M. E. Mann acknowledges support from the Alexander Hollaender Distinguished Postdoctoral Research Fellowship program of the Department of Energy. We thank P. D. Jones for providing the East Anglia surface temperature anomaly data, and we thank K. Trenberth and an anonymous reviewer for comments on an earlier version of the manuscript.

References

- Allen, M. R., and L. A. Smith, 1994: Investigating the origins and significance of low-frequency modes of climatic variability. *Geophys. Res. Lett.*, **21**, 883–886.
- Balling, R. C., 1992: The heated debate: Greenhouse predictions versus climate reality. Pacific Res. Inst. for Public Policy, San Francisco, Calif.

- Barnett, T. P., 1991: The interaction of multiple time scales in the tropical climate system. *J. Clim.*, **4**, 269–281.
- Battisti, D. S., 1990: Interannual variability in coupled tropical atmosphere-ocean models. *Climate-Ocean Interaction*, edited by M. E. Schlesinger, Kluwer Acad., Norwell, Mass., 127–160.
- Bear, L. K., and G. L. Pavlis, 1997: Estimation of slowness vectors and their uncertainties using multi-wavelet seismic array processing. *Bull. Seismol. Soc. Am.*, **87**, 755–769.
- Bjerknes, J., 1969: Atmospheric teleconnections from the Equatorial Pacific. *Mon. Weather Rev.*, **97**, 163–172.
- Bloomfield, P., 1976: *Fourier Analysis of Time Series: An Introduction*. John Wiley, New York.
- Borisenkov, Y. P., 1992: Documentary evidence from the U.S.S.R.. *Climate Since 1500 A.D.*, edited by R. S. Bradley and P. D. Jones, Routledge, London, 171–183.
- Bottomley, M., C. K. Folland, J. Hsiung, R. E. Newell, and D. E. Parker, 1990: Global ocean surface temperature atlas (GOSTA). Joint Meteorol. Off. and Mass. Inst. of Technol. Proj., U.K. Dep. of the Environ. and Energy, HMSO, London.
- Cane, M. A., A. C. Clement, A. Kaplan, Y. Kushnir, D. Pozdnyakov, R. Seager, S. E. Zebiak, and R. Murtugudde, 1997: Twentieth-century sea surface temperature trends. *Science*, **275**, 957–960.
- Cayan, D. R., and R. H. Webb, 1992: El Niño/Southern Oscillation and streamflow in the western United States. *El Niño: Historical and Paleoclimatic Aspects of the Southern Oscillation*, edited by H. F. Diaz and V. Markgraf, Cambridge Univ. Press, New York, 29–68.
- Chang, P., and S. G. H. Philander, 1994: A coupled ocean-atmosphere instability of relevance to the seasonal cycle. *J. Atmos. Sci.*, **24**, 3627–3648.
- Chelton, D. B., and M. G. Schlax, 1996: Global observations of oceanic Rossby waves. *Science*, **272**, 234–238.
- D'Arrigo, R. D., and G. C. Jacoby, 1992: A tree-ring reconstruction of New Mexico winter precipitation and its relation to El Niño/Southern Oscillation events, in. *El Niño: Historical and Paleoclimatic Aspects of the Southern Oscillation*, edited by H. F. Diaz and V. Markgraf, Cambridge Univ. Press, New York, 243–257.
- Daubechies, I., 1992: *Ten Lectures on Wavelets*. SIAM Press, Philadelphia, Pa.

- Delworth, T., Manabe, S., and R. J. Stouffer, 1993: Interdecadal variations of the thermohaline circulation in a coupled ocean-atmosphere model. *J. Clim.*, **6**, 1993–2011.
- Deser, C., and M. Blackmon, 1993: Surface climate variations over the North Atlantic ocean during winter: 1900–1989. *J. Clim.*, **6**, 1743–1753.
- Dunbar, R. B., Wellington, G. M., Colgan, M. W., and P. W. Glynn, 1994: Eastern Pacific sea surface temperature since 1600 A.D.: The $\delta^{18}\text{O}$ record of climate variability in Galapagos corals. *Paleoceanography*, **9**, 291–315.
- Elliot, W. P., and J. K. Angell, 1988: Evidence for changes in Southern Oscillation relationships during the last 100 years. *J. Clim.*, **1**, 729–737.
- Ghil, M., and R. Vautard, 1991: Interdecadal oscillations and the warming trend in global temperature time series. *Nature*, **350**, 324–327.
- Goddard, L., and N. E. Graham, 1997: El Niño in the 1990s. *J. Geophys. Res.*, **102**, 10423–10436.
- Graham, N. E., 1994: Decadal-scale climate variability in the tropical and North Pacific during the 1970s and 1980s: Observations and model results. *Clim. Dyn.*, **10**, 135–162.
- Graham, N. E., 1995: Simulation of recent global temperature trends. *Science*, **267**, 666–671.
- Groisman, P. Y., 1992: Possible regional climate consequences of the Pinatubo eruption: An empirical approach. *Geophys. Res. Lett.*, **19**, 1603–1606.
- Gu, D., and S. G. H. Philander, 1995: Secular changes of annual and interannual variability in the tropics during the past century. *J. Clim.*, **8**, 864–876.
- Gu, D., and S. G. H. Philander, 1997: Interdecadal climate fluctuations that depend on exchanges between the tropics and extratropics. *Science*, **275**, 805–807.
- Halpert, M. S., and C. F. Ropelewski, 1992: Surface temperature patterns associated with the Southern Oscillation. *J. Clim.*, **5**, 577–593.
- Hegerl, G. C., K. Hasselmann, U. Cubasch, J. F. B. Mitchell, E. Roeckner, R. Voss., and J. Waszkewitz, 1997: Multi-fingerprint detection and attribution analysis of greenhouse gas, greenhouse gas-plus-aerosol and solar forced climate change. *Clim. Dyn.*, **13**, 613–634.
- Intergovernmental Panel on Climate Control (IPCC), 1996: *Climate Change 1995, The Science of Climate Change*. edited by J.T. Houghton et al., Cambridge Univ. Press,

New York.

- Jones, P. D., and R. S. Bradley, 1992: Climate variations in the longest instrumental records. *Climate Since 1500 A.D.*, edited by R. S. Bradley and P. D. Jones, Routledge, London, 246–268.
- Jones, P. D., and K. R. Briffa, 1992: Global surface air temperature variations during the 20th century, 1, Spatial, temporal and seasonal details. *Holocene*, **1**, 165–179.
- Karl, T. R., R. W. Knight, D. R. Easterling, and R. G. Quayle, 1995: Trends in US climate during the twentieth century. *Consequences*, **1**, no. 1, Spring. [Available on-line from <http://gcrio.ciesin.org/CONSEQUENCES/spring95/Climate.html>.]
- Kelly, P. M., P. D. Jones, and J. Pengqun, 1996: The spatial response of the climate system to explosive volcanic eruptions. *Int. J. Climatol.*, **16**, 537–550.
- Kerr, R., 1995: US climate tilts toward the greenhouse. *Science*, **268**, 363–364.
- Kessler, W. S., and M. J. McPhaden, 1995: Oceanic equatorial waves and the 1991–1993 El Niño. *J. Clim.*, **8**, 1757–1774.
- Knutson, T. R., S. Manabe, and D. Gu, 1997: Simulated ENSO in a global atmosphere-ocean model: Multidecadal amplitude modulation and CO₂ sensitivity. *J. Clim.*, **10**, 138–161.
- Kuo, C., Lindberg, C., and D. J. Thomson, 1990: Coherence established between atmospheric carbon dioxide and global temperature. *Nature*, **343**, 709–713.
- Kushnir, Y., 1994: Interdecadal variations in North Atlantic sea surface temperature and associated atmospheric conditions. *J. Clim.*, **7**, 141–157.
- Labitzke, K., and H. van Loon, 1988: Associations between the 11-year solar cycle, the QBO, and the atmosphere, I, The troposphere and stratosphere in the northern hemisphere in winter. *J. Atmos. Terr. Phys.*, **50**, 197–206.
- Latif, M., and T. P. Barnett, 1994: Causes of decadal climate variability over the North Pacific and North America. *Science*, **266**, 634–637.
- Lean, J., J. Beer, and R. S. Bradley, 1995: Comparison of proxy records of climate change and solar forcing. *Geophys. Res. Lett.*, **22**, 3195–3198.
- Lilly, J., and J. Park, 1995: Multiwavelet spectral and polarization analysis of seismic records. *Geophys. J. Int.*, **122**, 1001–1021.
- Lough, J. M., 1992: An index of the Southern Oscillation reconstructed from western North American tree-ring chronologies. *El Niño: Historical and Paleoclimatic*

Aspects of the Southern Oscillation, edited by H. F. Diaz and V. Markgraf, Cambridge Univ. Press, New York, 215–226.

- Mann, M. E., and J. Lees, 1996: Robust estimation of background noise and signal detection in climate time series. *Clim. Change*, **33**, 409–445.
- Mann, M. E., and J. Park, 1993: Spatial correlations of interdecadal variation in global surface temperatures. *Geophys. Res. Lett.*, **20**, 1055–1058.
- Mann, M. E., and J. Park, 1994: Global-scale modes of surface temperature variability on interannual to century timescales. *J. Geophys. Res.*, **99**, 25819–25833.
- Mann, M. E., and J. Park, 1996: Joint spatialtemporal modes of surface temperature and sea-level pressure variability in the Northern Hemisphere during the last century. *J. Clim.*, **9**, 2137–2162.
- Mann, M. E., and J. Park, 1999: Oscillatory spatiotemporal signal detection in climate studies. *Adv. Geophys.*, **41**, 1–131.
- Mann, M. E., J. Park, and R. Bradley, 1995: Global interdecadal and century-scale climate oscillations during the last half millennium. *Nature*, **378**, 266–270.
- Mann, M. E., R. S. Bradley, and M. K. Hughes, 1998: Global-scale temperature patterns and climate forcing over the past six centuries. *Nature*, **393**, 779–787.
- Mann, M. E., R. S. Bradley, and M. K. Hughes, 1999: Long-term variability in the El Niño Southern Oscillation and associated teleconnections. *El Niño and the Southern Oscillation: Multiscale Variability and Its Impacts on Natural Ecosystems and Society*, edited by H. F. Diaz and V. Markgraf, Cambridge Univ. Press, New York, in press.
- Meehl, G. A., and W. M. Washington, 1996: El Niño-like climate change in a model with increased atmospheric CO₂ concentrations. *Nature*, **382**, 56–60.
- Mehta, V. M., and T. Delworth, 1995: Decadal variability in the tropical Atlantic Ocean surface temperature in shipboard measurements and a global ocean-atmosphere model. *J. Clim.*, **8**, 172–190.
- Park, J., Lindberg, C. R., and F. L. Vernon III, 1987: Multitaper spectral analysis of high-frequency seismograms. *J. Geophys. Res.*, **92**, 12675–12684.
- Petersen, G., 1935: Estudios climatologicos del noroeste Peruana. *Boll. Soc. Geol. Peru*, **7**, 1–141.
- Philander, S. G., 1990: *El Niño, La Niña, and the Southern Oscillation*. Academic, San

Diego, Calif.

- Quinn, W. H., and V. T. Neal, 1992: The historical record of El Niño events. *Climate Since 1500 A.D.*, edited by R. S. Bradley and P. D. Jones, Routledge, London, 623–648.
- Rajagopalan, B., U. Lall, and M. A. Cane, 1997: Anomalous ENSO occurrences: An alternative view. *J. Clim.*, **10**, 2351–2357.
- Robertson, 1996: Interdecadal variability in a multicentury climate integration. *Clim. Dyn.*, **12**, 227–241.
- Robock, A., and J. Mao, 1992: Winter warming from large volcanic eruptions. *Geophys. Res. Lett.*, **12**, 2405–2408.
- Ropelewski, and Halpert, 1987: Global and regional scale precipitation patterns associated with the El Niño-Southern Oscillation. *Mon. Weather Rev.*, **115**, 1606–1626.
- Schlesinger, M. E., and N. Ramankutty, 1994: An oscillation in the global climate system of period 65–70 years. *Nature*, **367**, 723–726.
- Simkin, T., and L. Siebert, 1994: *Volcanoes of the World*, 2nd ed. Geoscience Press, Tucson, Ariz.
- Thomson, D. J., 1982: Spectrum estimation and harmonic analysis. *IEEE Proc.*, **70**, 1055–1096.
- Thompson, L. G., E. Mosley-Thompson, and P. A. Thompson, 1992: Reconstructing interannual climate variability from subtropical and tropical ice-core records. *El Niño: Historical and Paleoclimatic Aspects of the Southern Oscillation*, edited by H. F. Diaz and V. Markgraf, Cambridge Univ. Press, New York, 295–322.
- Trenberth, K. E., 1984: Signal versus noise in the Southern Oscillation. *Mon. Weather Rev.*, **112**, 326–332.
- Trenberth, K. E., 1990: Recent observed interdecadal climate changes in the northern hemisphere. *Bull. Am. Meteorol. Soc.*, **71**, 988–993.
- Trenberth, K. E., 1996: El Niño-Southern Oscillation. *Climate Change: Developing Southern Hemisphere Perspectives*, edited by T. W. Giambelluca and A. Henderson-Sellers, John Wiley, New York, 145–173.
- Trenberth, K. E., and T. J. Hoar, 1996: The 1990–1995 El Niño-Southern Oscillation event: Longest on record. *Geophys. Res. Lett.*, **23**, 57–60.
- Trenberth, K. E., and Hurrell, 1994: Decadal atmosphere-ocean variations in the Pacific.

Clim. Dyn., **9**, 303–319.

Trenberth, K. E., and D. J. Shea, 1987: On the evolution of the Southern Oscillation. *Mon. Weather Rev.*, **115**, 3078–3096.

Walker, D. A., 1995: More evidence indicates link between El Niños and seismicity. *Eos Trans. AGU*, **76**, 33–36.

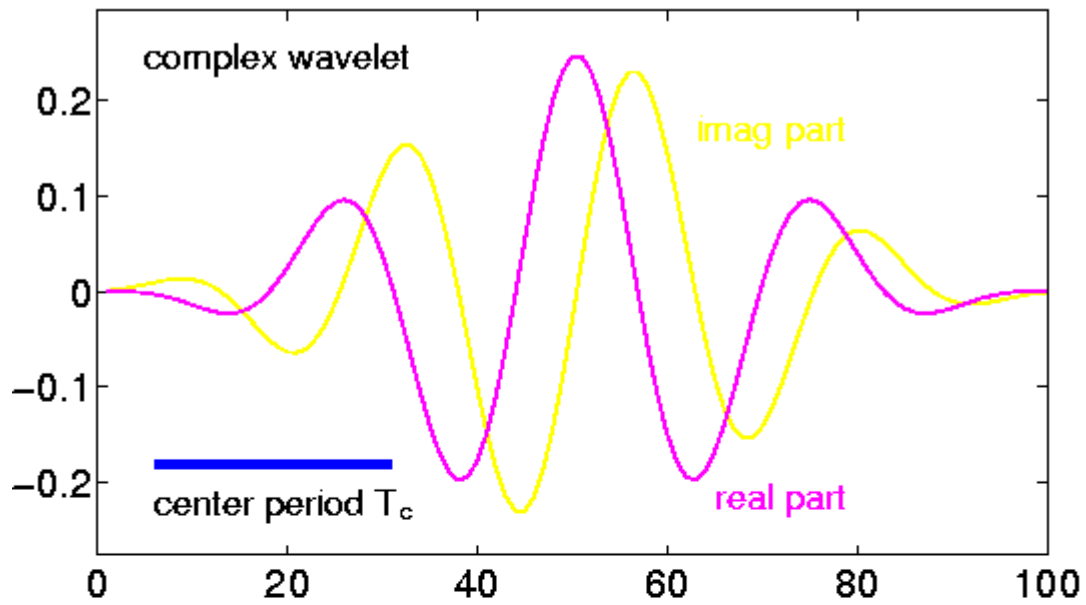
Wang, B., and Y. Wang, 1996: Temporal structure of the Southern Oscillation as revealed by waveform and wavelet analysis. *J. Clim.*, **9**, 1586–1598.

RECEIVED: 5 March 1997

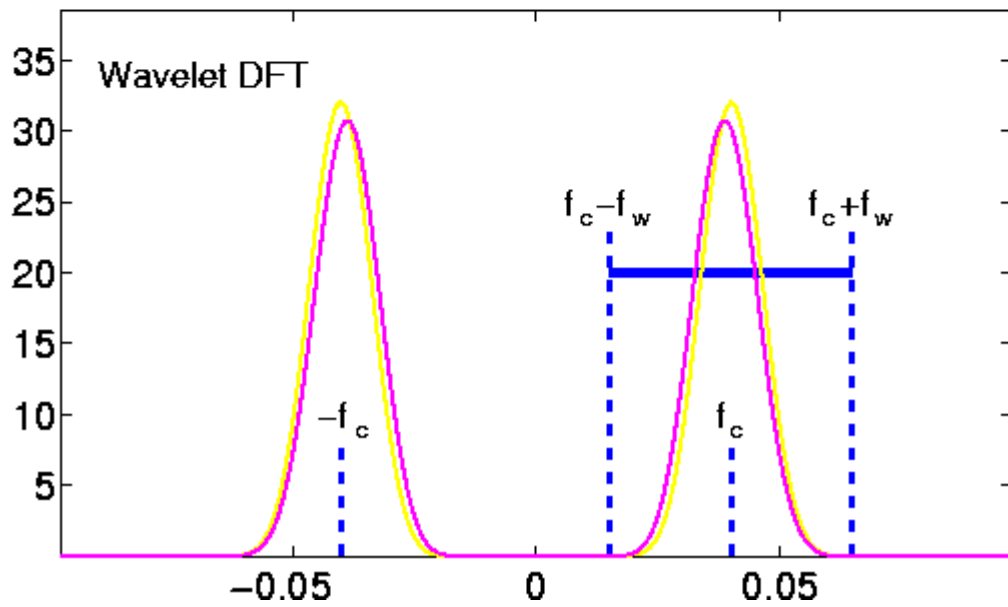
ACCEPTED: 24 March 1999

¹ *Earth Interactions* is published jointly by the [American Meteorological Society](#), the [American Geophysical Union](#), and the [Association of American Geographers](#). Permission to use figures, tables, and *brief* excerpts from this journal in scientific and educational works is hereby granted provided that the source is acknowledged. Any use of material in this journal that is determined to be “fair use” under Section 107 or that satisfies the conditions specified in Section 108 of the U.S. Copyright Law (17 USC, as revised by P.L. 94–553) does not require the publishers' permission. For permission for any other form of copying, contact one of the copublishing societies.

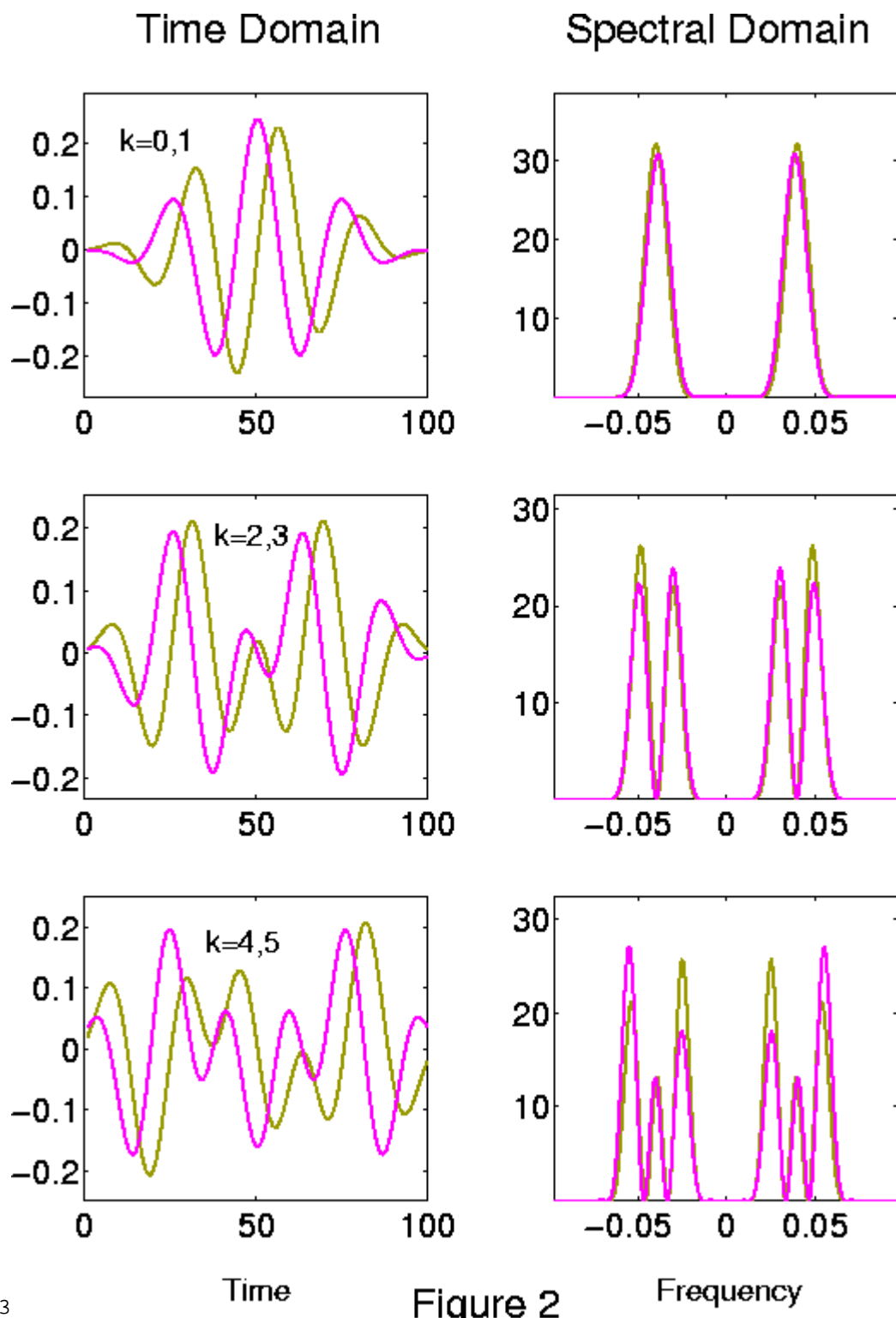
Time Domain



Spectral Domain **Figure 1**



2



3

Multiwavelet Correlation Detection

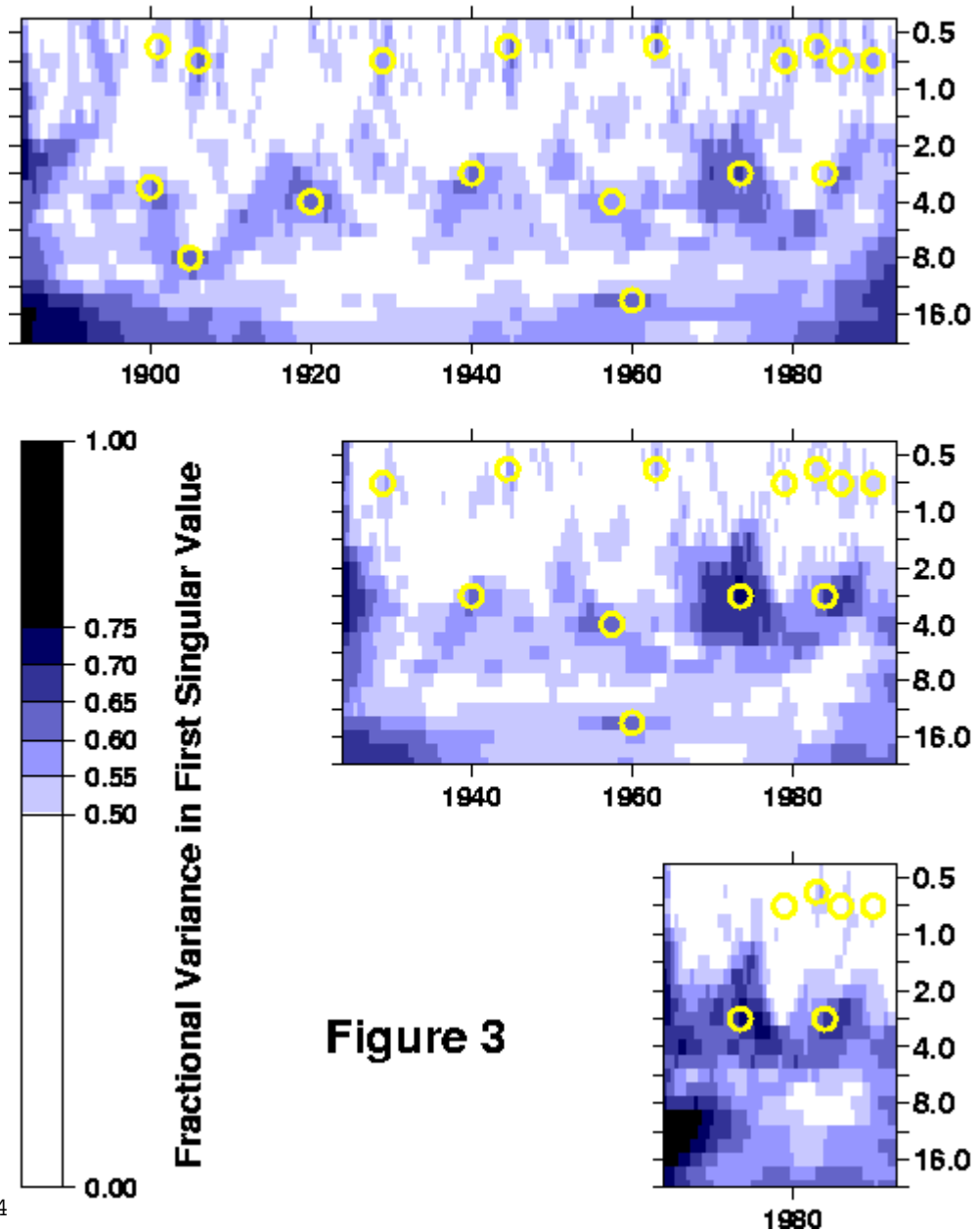


Figure 3

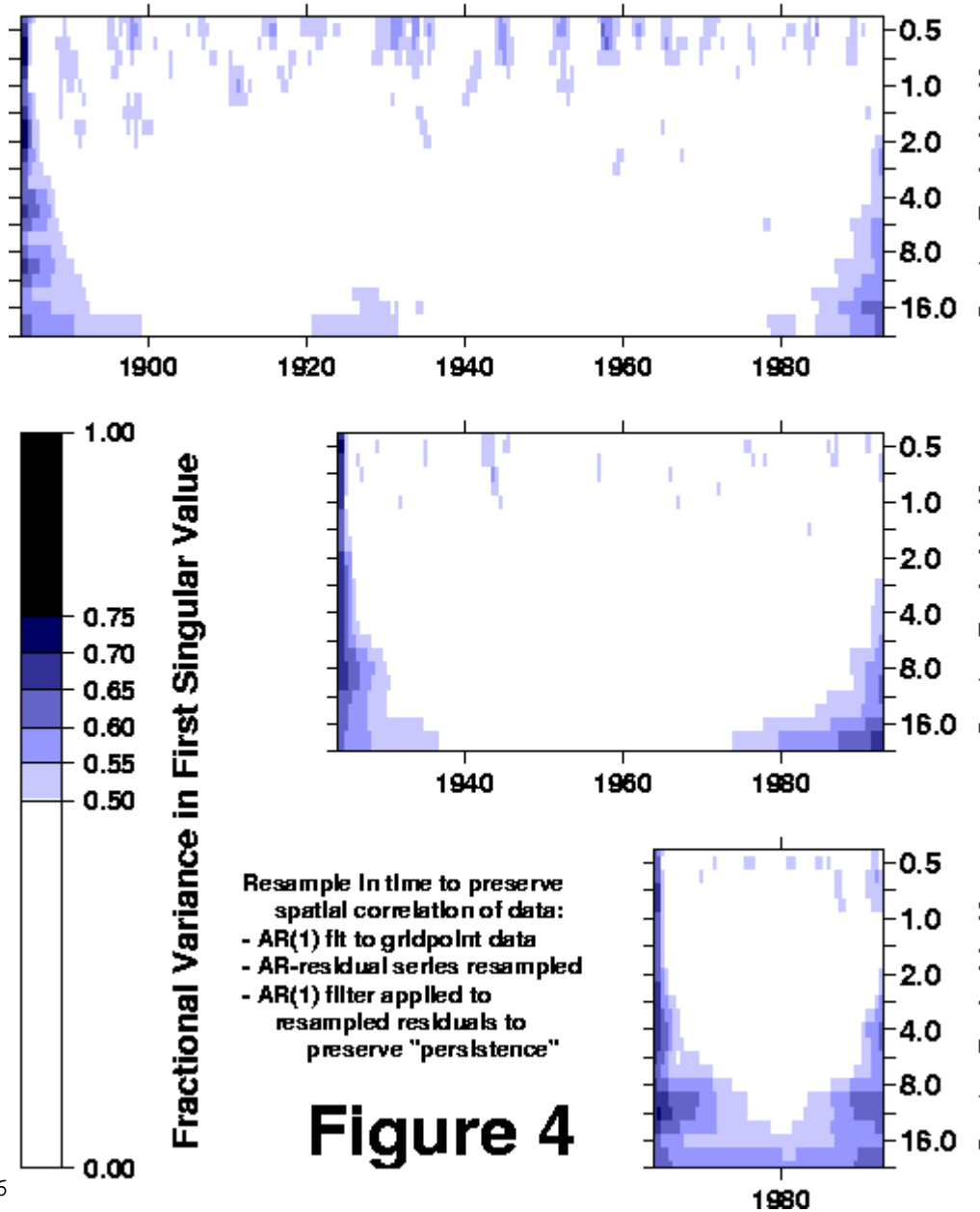
⁵Table 1. Statistically significant interannual and decadal signals in the 20th century isolated in the wavelet analysis: Amplitudes of variability (in °C) correspond to peak-to-peak variation at a grid point or in a global average.

Center Year	T (years)	$\bar{d}^{(1)}$	Grid Points	T_{RMS}	T_{GLB}	T_{NH}
1900	3.4	0.63	368	0.70	0.24	0.24
1920	4.0	0.67	500	1.13	0.48	0.51
1940	2.8	0.63	663	0.84	0.05	0.02
1957.5	4.0	0.62	898	0.78	0.27	0.30
1973.5	2.8	0.74	1570	1.01	0.41	0.42
1984	2.8	0.70	1570	0.94	0.21	0.18
1905	8.0	0.66	368	0.62	0.25	0.24
1960	14	0.65	663	0.59	0.21	0.16

Click on icon to

display TABLE1.

Random Resampling Test



6

⁷Table 2. Significant quasi-annual spatiotemporal signals in 20th century isolated in the wavelet analysis (continuous 1884–1993 dataset): Amplitudes of variability (in °C) correspond to peak-to-peak variation at a grid point or in a global average.

Although the normalized first singular value $\tilde{d}^{(1)}$ is referenced to the continuous 1884–1993 dataset, for more recent episodes we use data from shorter time intervals, with more grid points, to calculate T_{RMS} and T_{GLB} .

Center Year	T (years)	$d^{(1)}$	Grid Points	T_{RMS}	T_{GLB}	Grid Points
1901	0.6	0.60	368	1.69	0.37	368
1906	0.7	0.65	368	1.75	0.40	368
1929	0.7	0.60	368	1.83	0.42	663
1944.5	0.6	0.63	368	2.06	0.06	663
1963.5	0.6	0.61	368	2.19	0.24	898
1979	0.7	0.59	368	1.16	0.09	1570
1983	0.6	0.60	368	1.49	0.32	1570
1986	0.6	0.58	368	1.35	0.20	1570
1990	0.7	0.58	368	1.72	0.20	1570

Click on icon

to display TABLE2.

8

Northern Hemisphere Temperature Anomaly

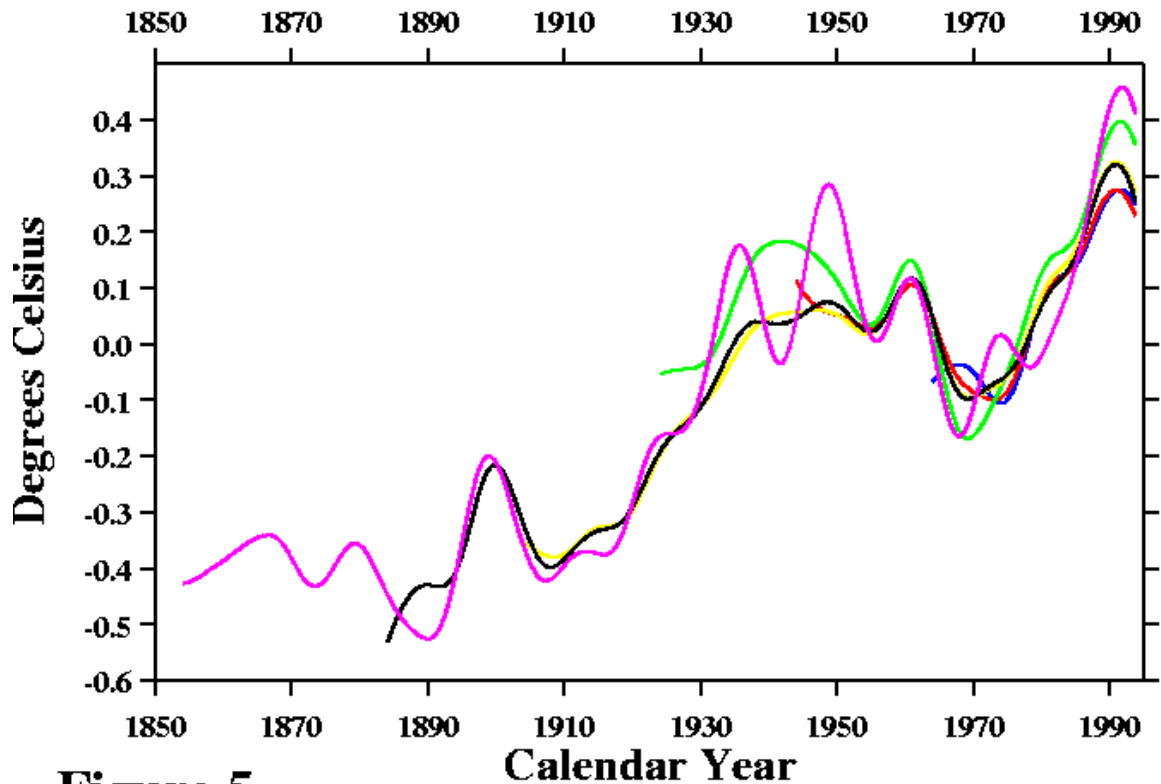


Figure 5

9

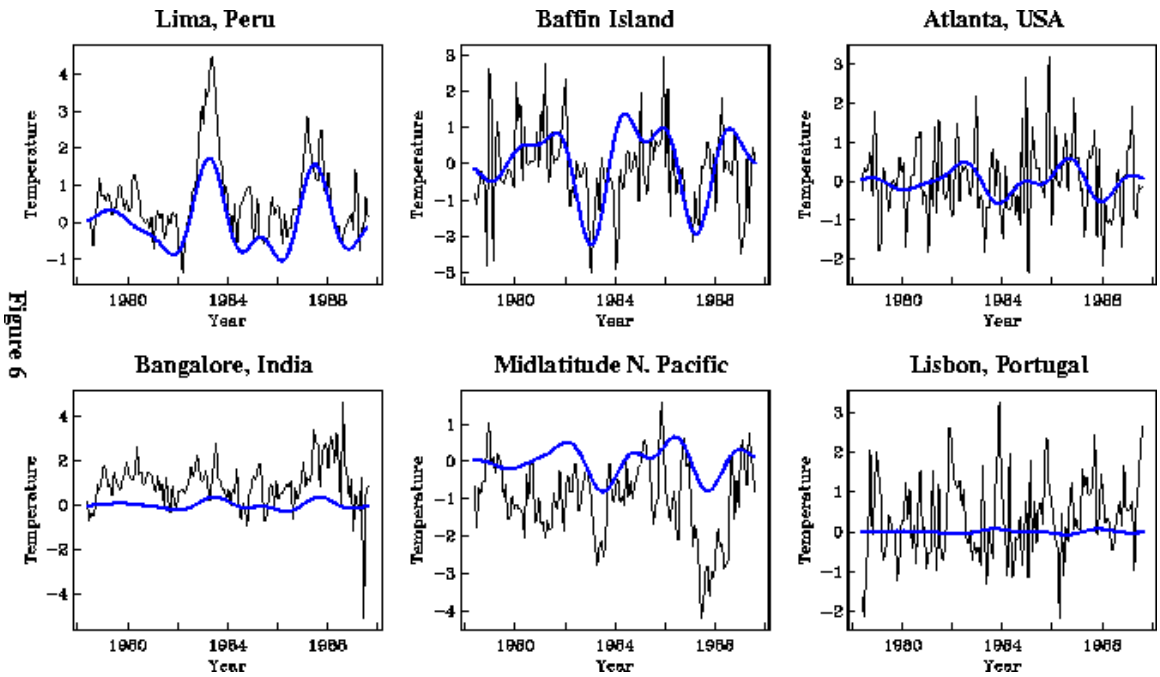


Figure 6

10

Center Time: 1984.0 Wavelet Period: 2.8 years

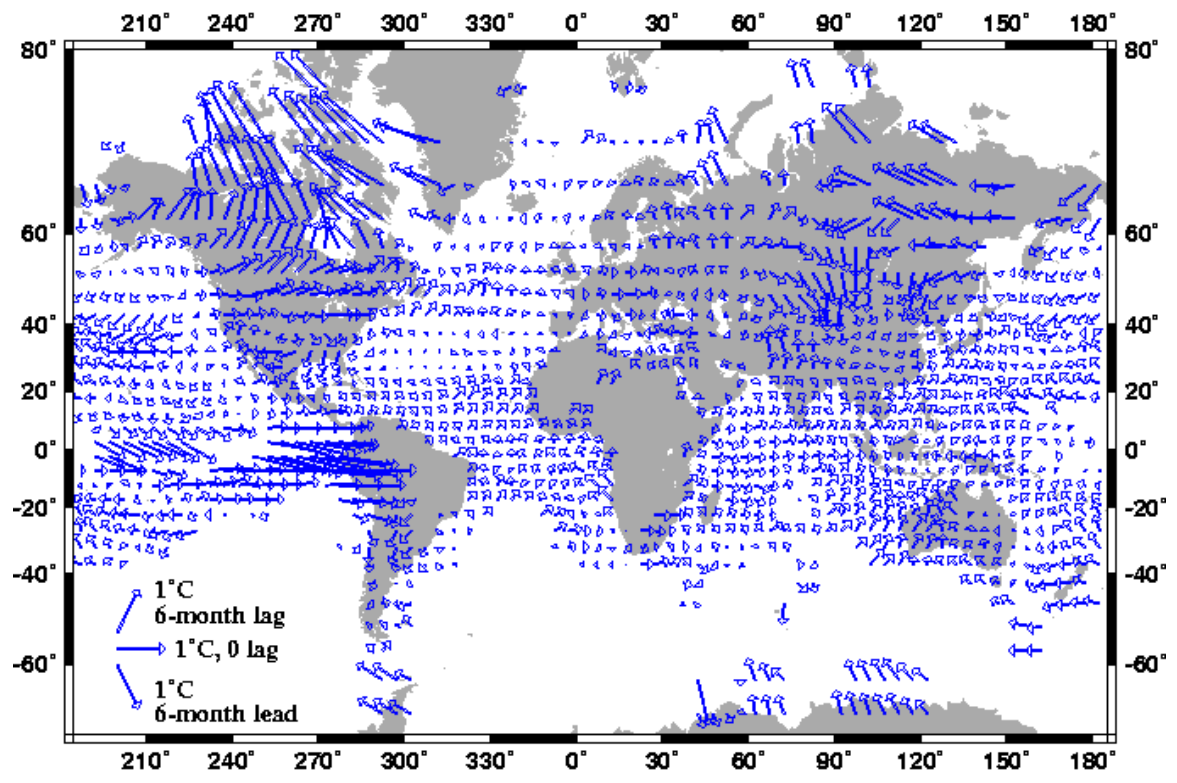


Figure 7

11

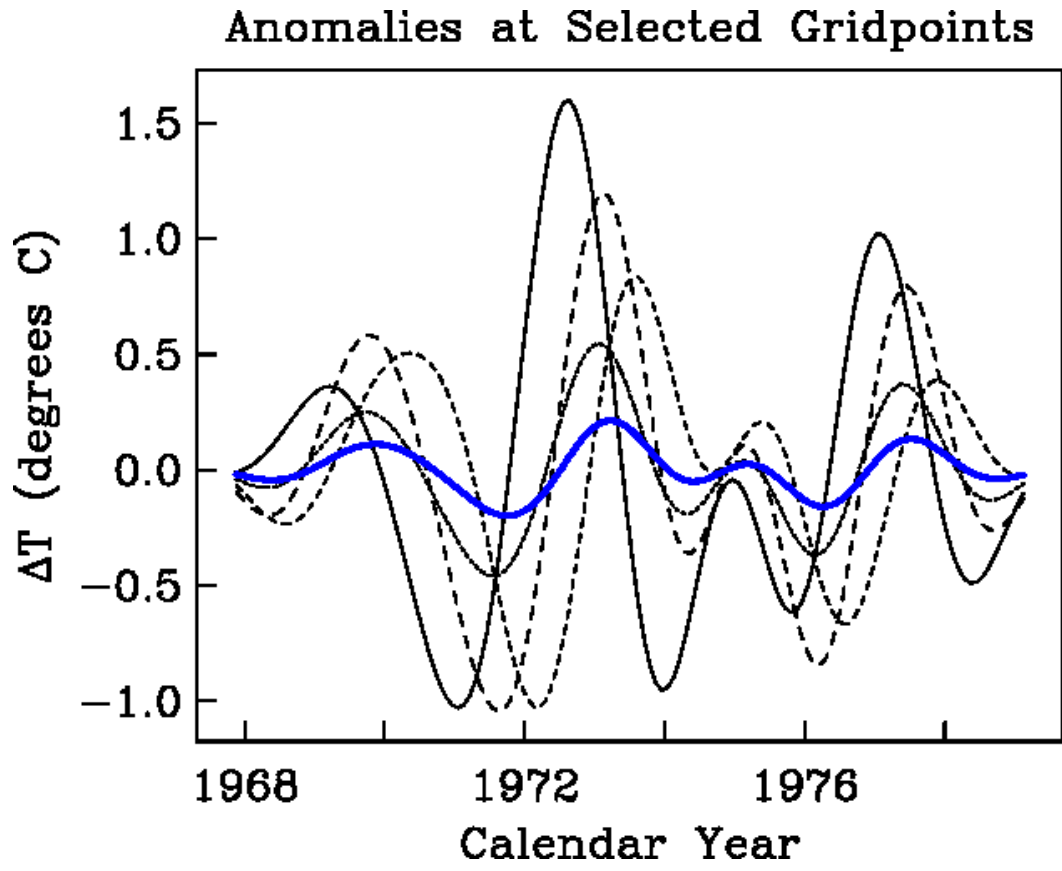


Figure 8

12

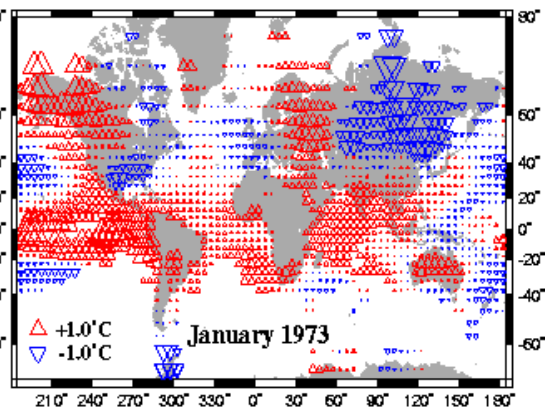
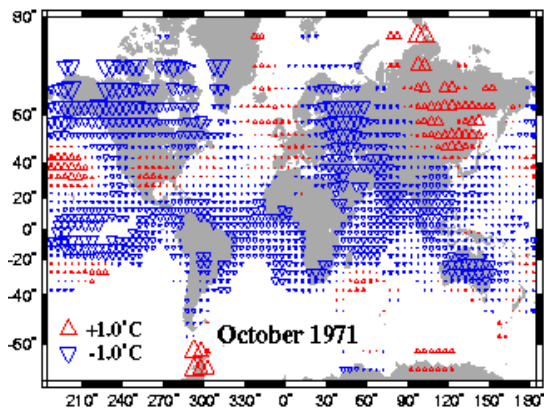
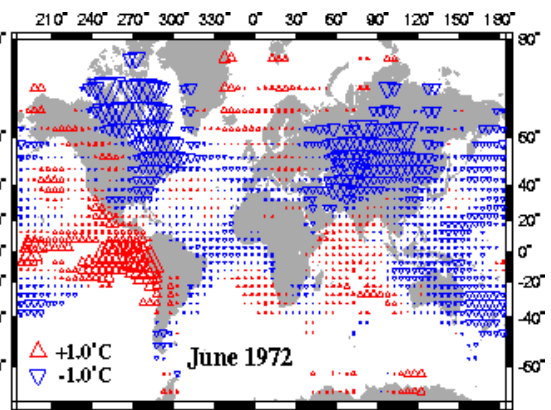
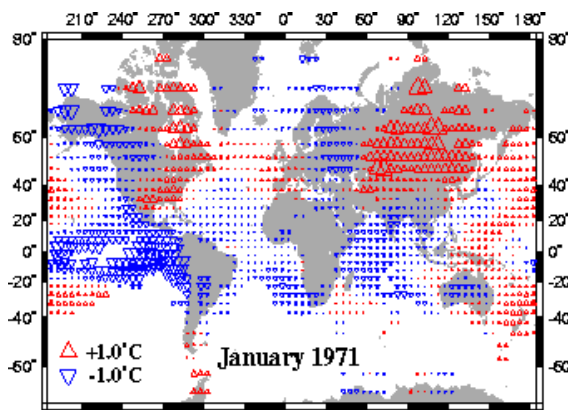


Figure 9a

Figure 9b

13

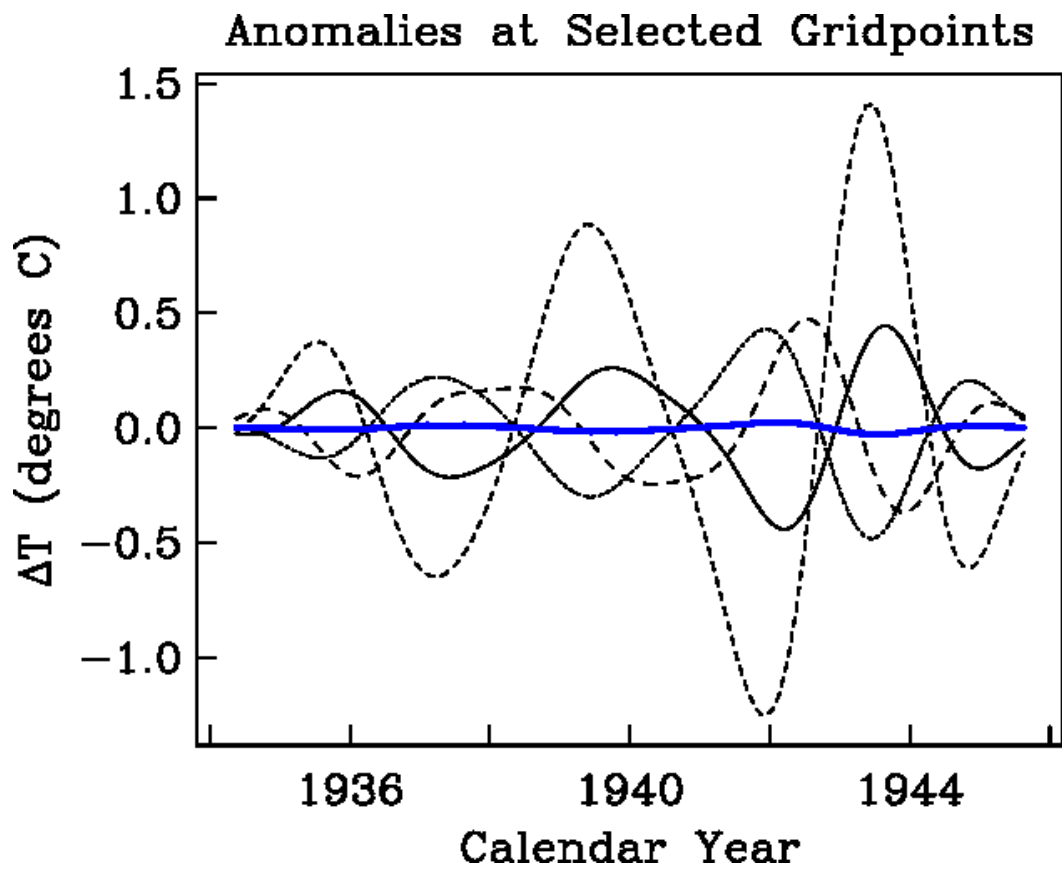


Figure 10

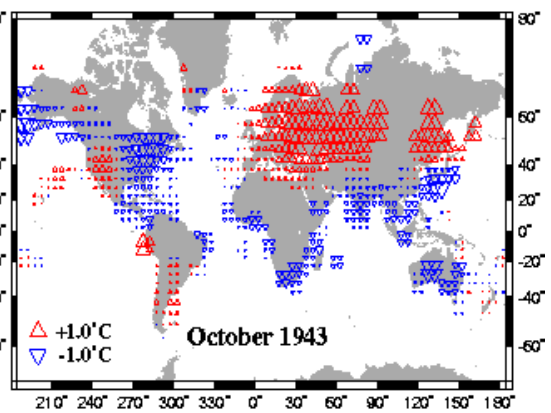
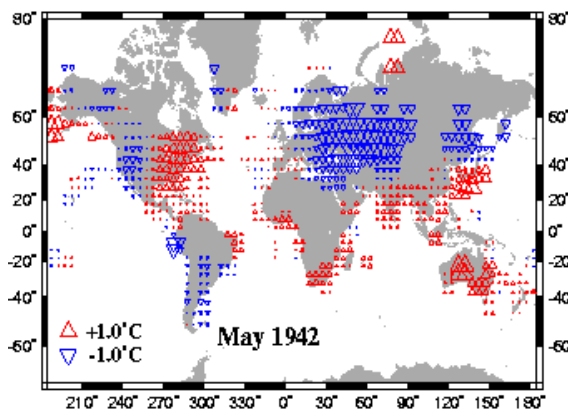
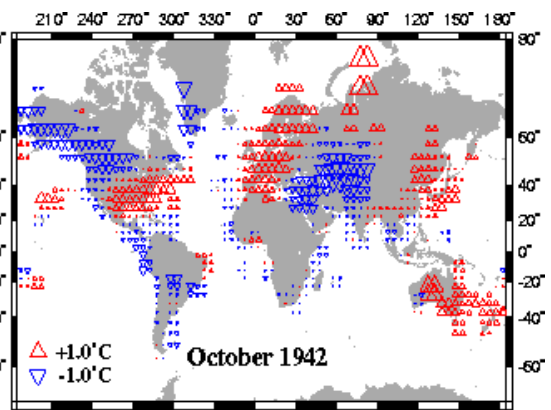
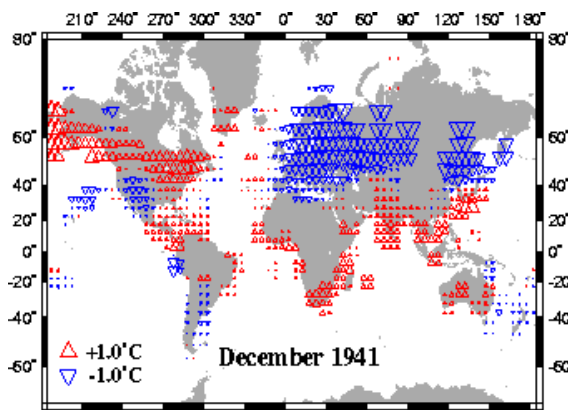


Figure 11a

Figure 11b

15

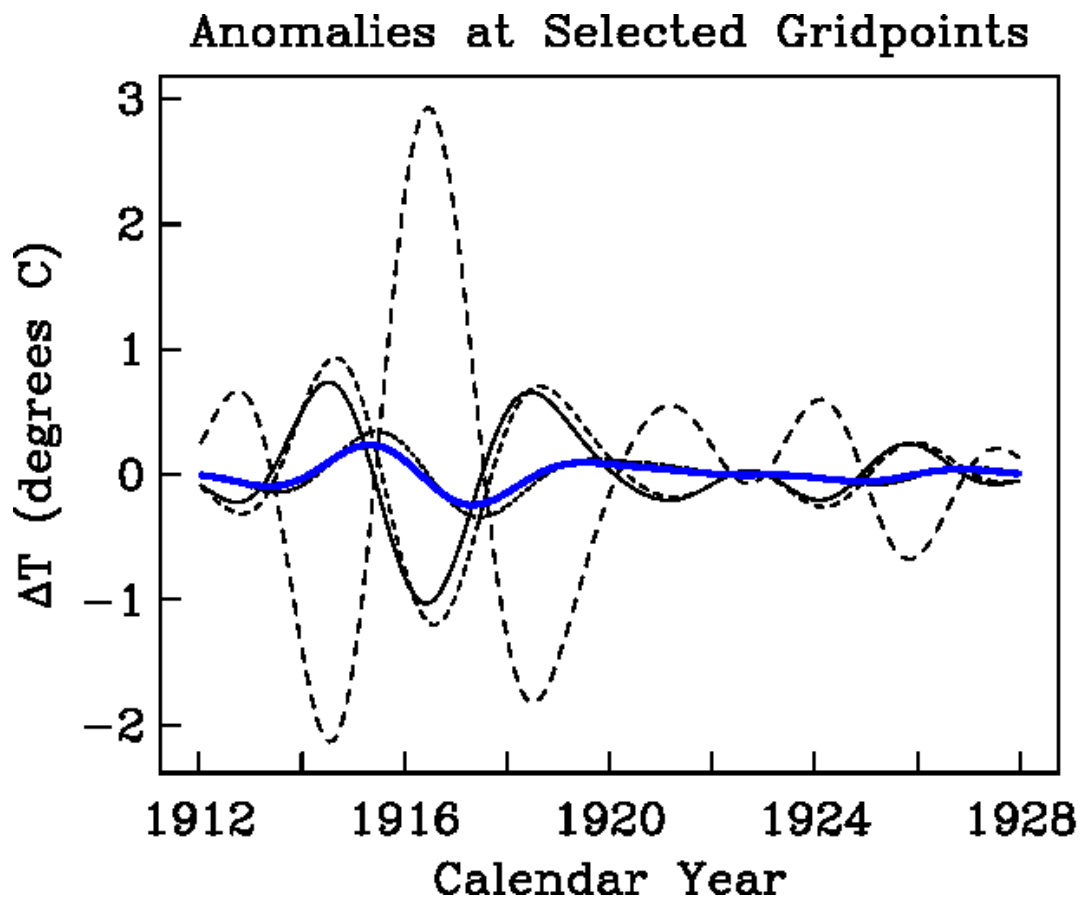


Figure 12

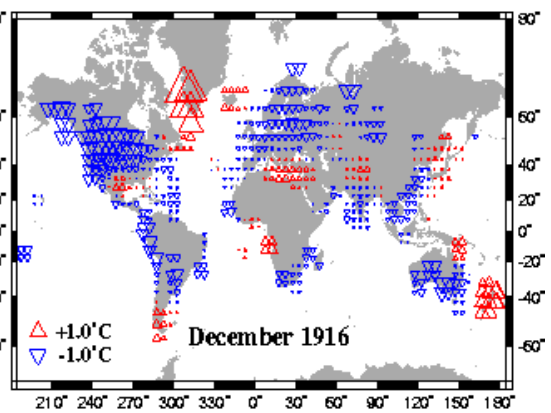
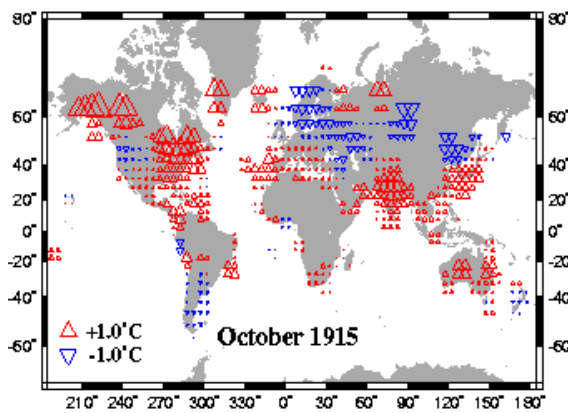
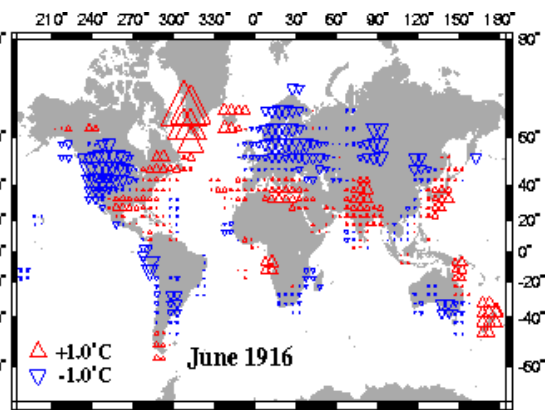
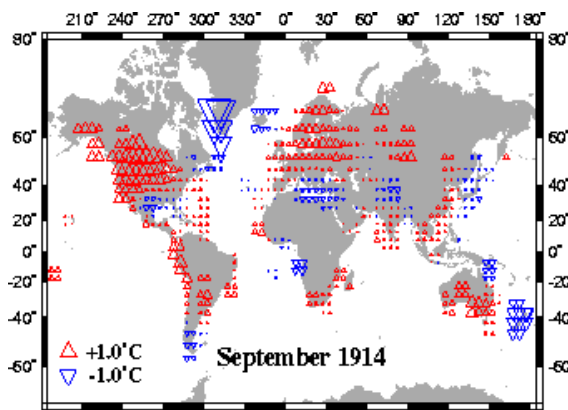
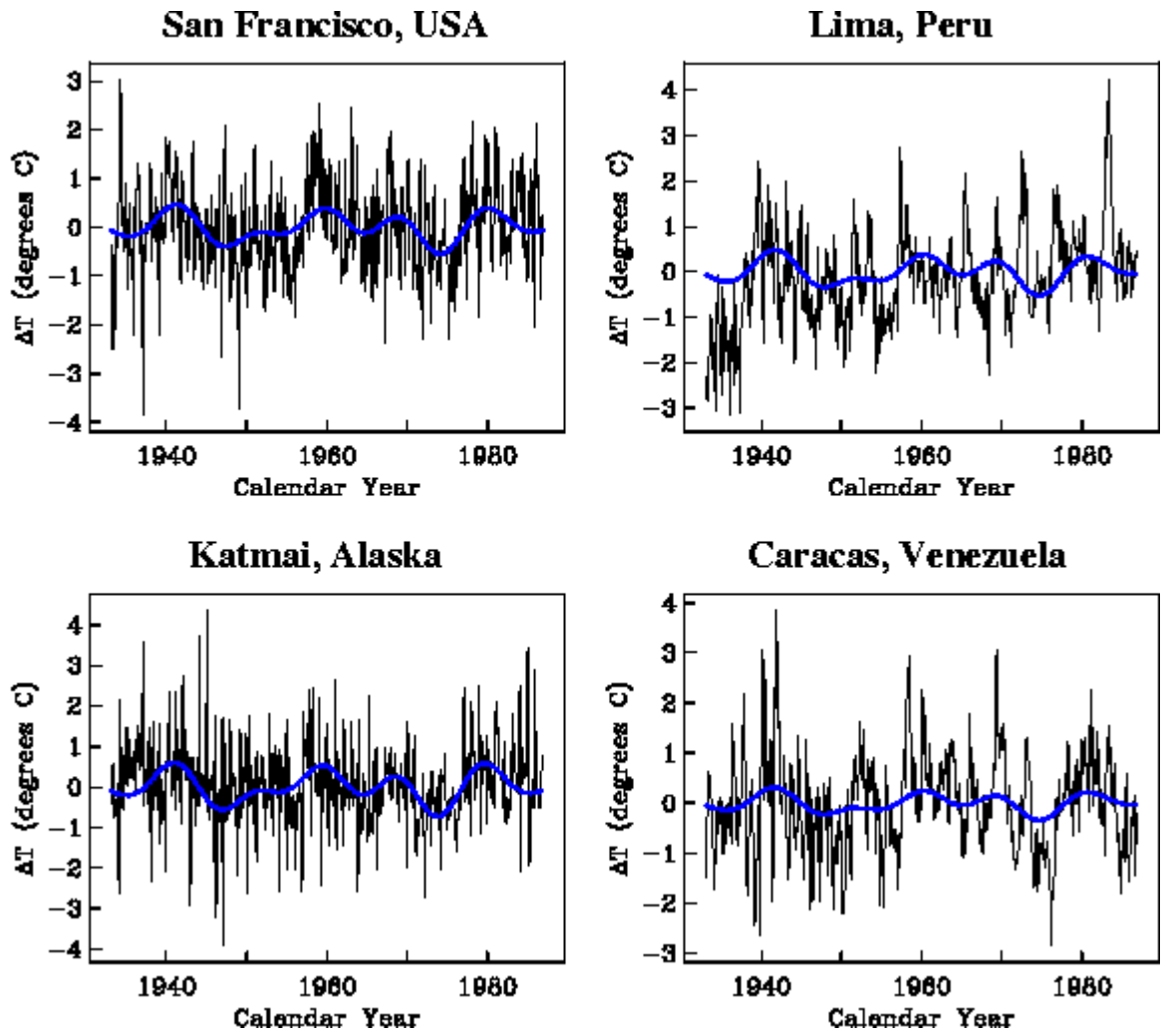


Figure 13a

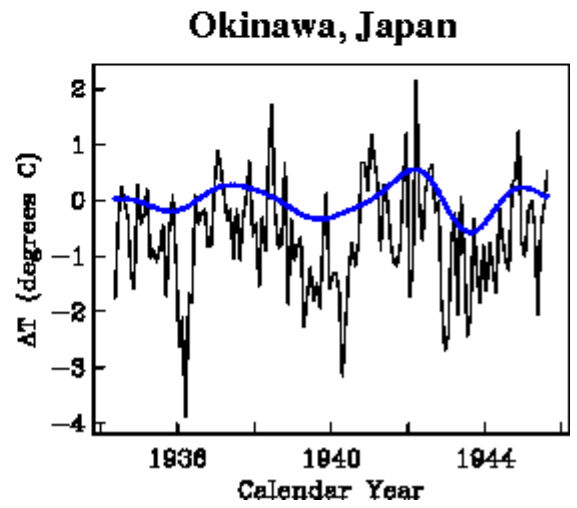
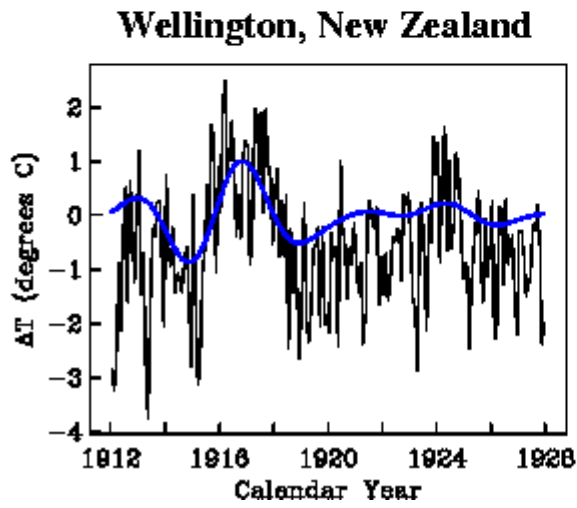
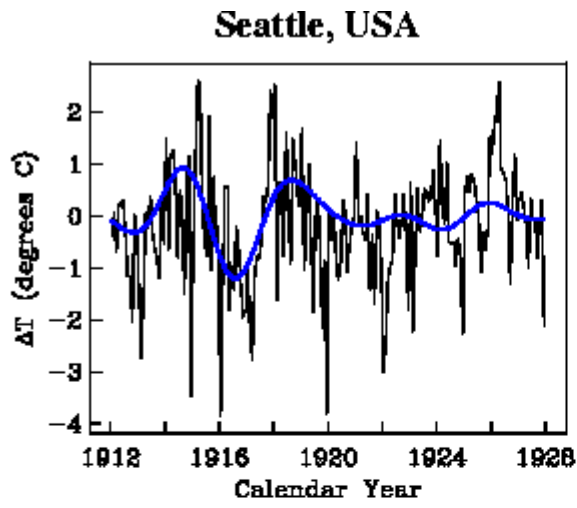
Figure 13b

Figure 14

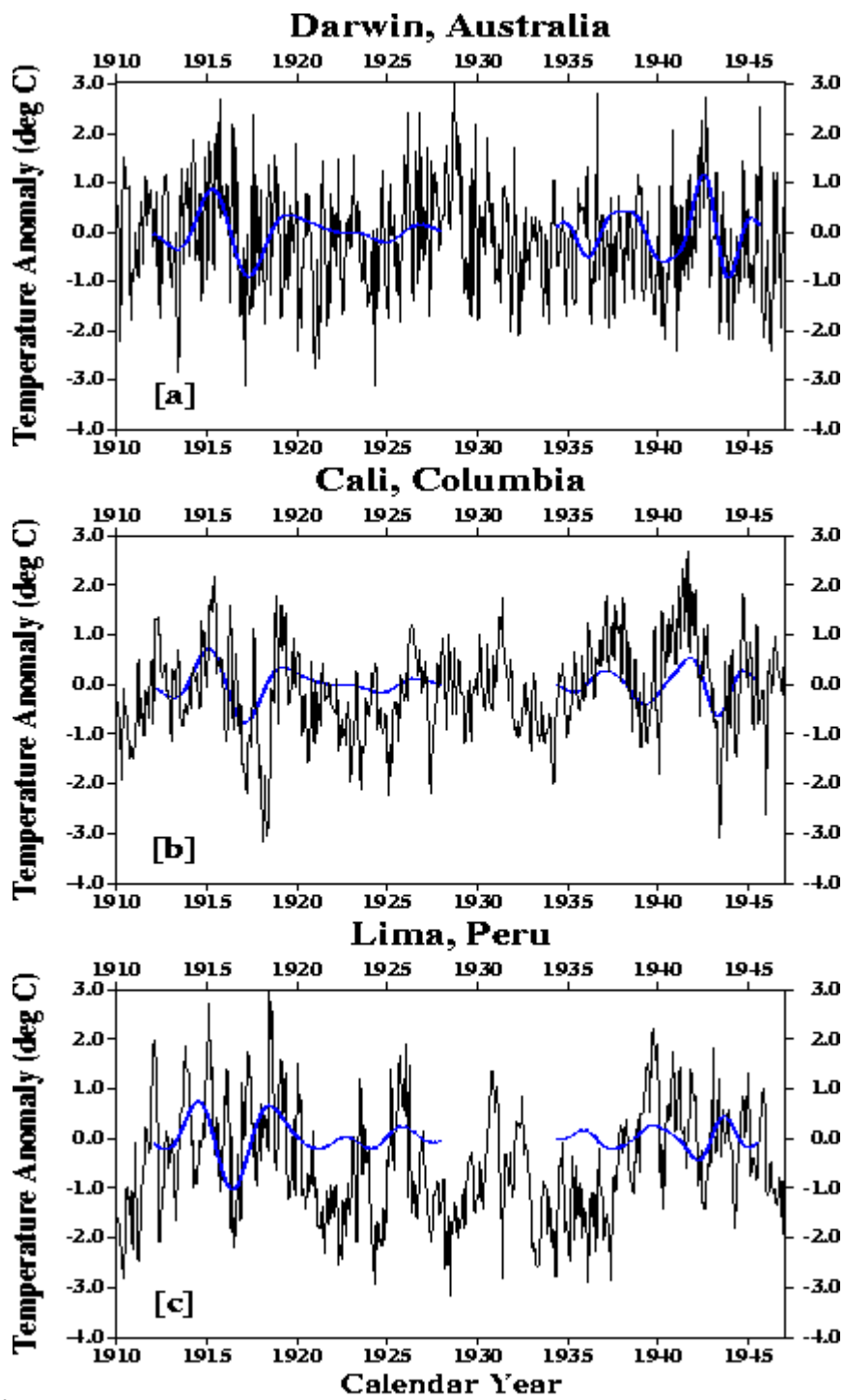


17

Figure 15



18



19 **Figure 16**

20

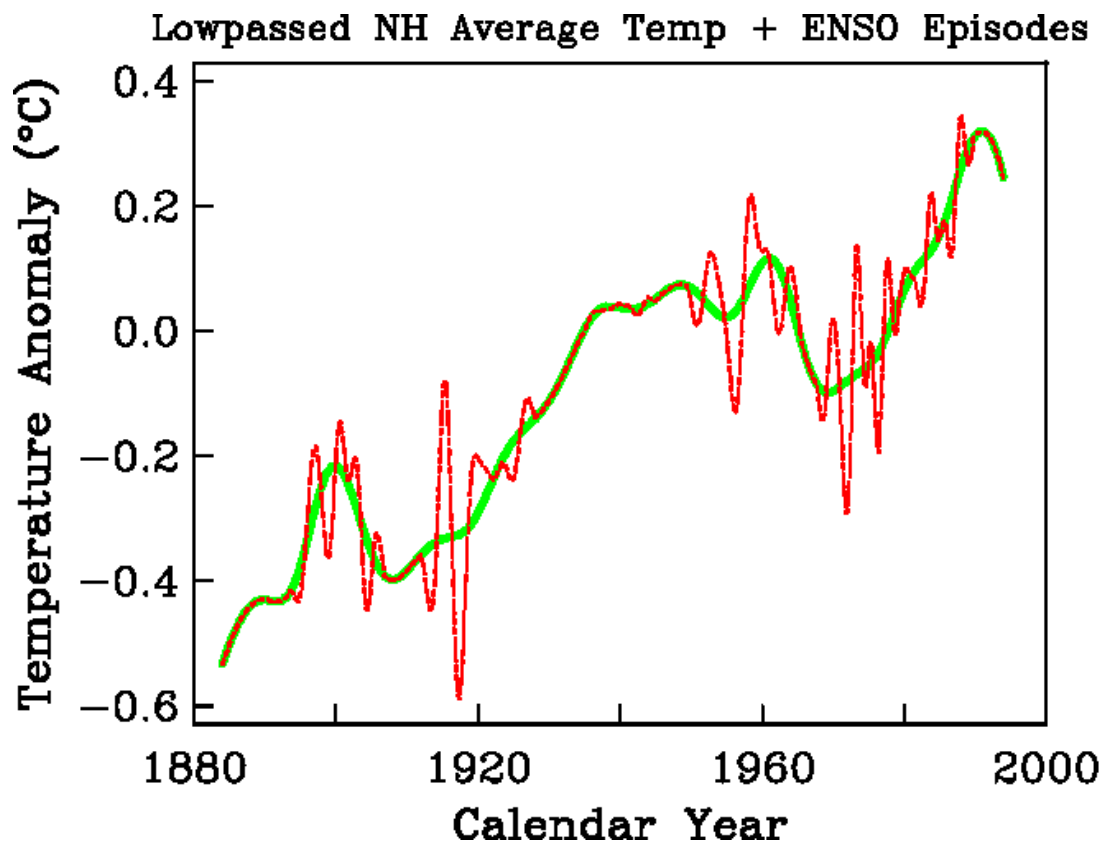


Figure 17